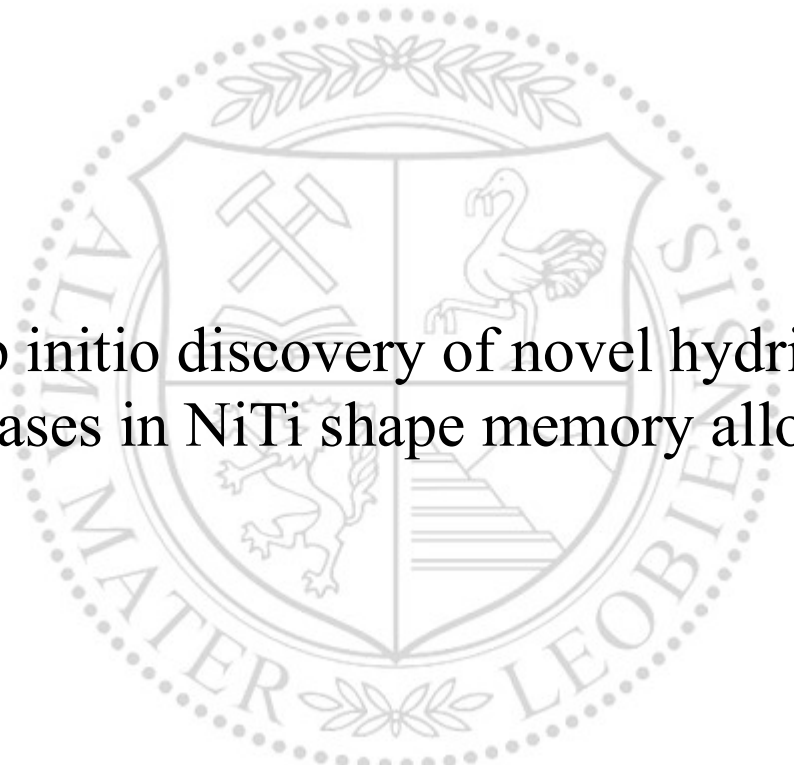




Chair of Physical Metallurgy

Master's Thesis



Ab initio discovery of novel hydride
phases in NiTi shape memory alloys

Anna Margarethe Paulik, BSc

February 2023

Ab initio discovery of novel hydride phases in NiTi shape memory alloys

Anna Margarethe Paulik

Abstract

The shape memory alloy NiTi is particularly popular for medical applications and implants due to its excellent biocompatibility and corrosion resistance. Detailed knowledge of its properties and interactions with other elements is crucial to ensure a safe and optimal application of the material. The focus of this work is the characterization of NiTi hydrides using the methods of density functional theory and the VASP code. Based on experimental observations, structural models have been created for different hydrogen concentrations and distributions. The formation energy has been calculated and compared between the models to find the most stable hydride structure. Furthermore, optimal cell parameters for a supercell which is stabilized in the B2 phase have been calculated using a manual fit and automated structural optimization. For some possible hydride structures, the elastic constants have been evaluated to assess mechanical stability. Diffraction patterns have been simulated and compared to experiments. Through the comparison of the different models, a few potentially mechanically and energetically stable structures could be identified. Furthermore, a phase transformation (change in cell shape) as a function of hydrostatic pressure (volume) has been predicted. Although pressure induced phase transformations have been reported for pure NiTi before, this analysis suggests that NiTiH exhibits a more complex behavior.

Ab Initio Untersuchungen von neuartigen Hydridphasen in NiTi Formgedächtnislegierungen

Anna Margarethe Paulik

Kurzfassung

Die Formgedächtnislegierung NiTi zeichnet sich durch ihre hervorragende Biokompatibilität und Korrosionsbeständigkeit für Anwendungen in der Medizintechnik, insbesondere als Implantatwerkstoff, aus. Kenntnis über seine Eigenschaften und Wechselwirkungen mit anderen Elementen sind entscheidend für eine sichere Anwendung des Materials. Diese Arbeit beschäftigt sich mit der Charakterisierung von NiTi-Hydriden unter Zuhilfenahme der Dichtefunktionaltheorie und des VASP-Codes. Basierend auf experimentellen Ergebnissen wurden Strukturmodelle für verschiedene Wasserstoffkonzentrationen und -verteilungen erstellt. Die Bildungsenergie wurde berechnet und mit den Strukturmodellen verglichen, um die stabilste Hydridstruktur zu finden. Darüber hinaus wurden die optimalen Gitterparameter für eine Supercelle, die in einer B2 Matrix stabilisiert ist, über eine manuelle und eine automatische Strukturoptimierung berechnet. Für einige der möglichen Hydridstrukturen wurden die elastischen Konstanten berechnet, um die mechanische Stabilität beurteilen zu können. Außerdem wurden Beugungsbilder simuliert und mit Experimenten verglichen. Durch den Vergleich der verschiedenen Modelle konnten einige potenziell mechanisch und energetisch stabile Strukturen identifiziert werden. Darüber hinaus wurde eine Phasenumwandlung (Formänderung der Einheitszelle) in Abhängigkeit des hydrostatischen Drucks (Volumen) vorhergesagt. Obwohl druckinduzierte Phasenumwandlungen bereits in reinem NiTi beobachtet wurden, legt diese Beobachtung die Vermutung nahe, dass NiTiH ein komplexeres Verhalten aufweist.



EIDESSTATTLICHE ERKLÄRUNG

Ich erkläre an Eides statt, dass ich diese Arbeit selbständig verfasst, andere als die angegebenen Quellen und Hilfsmittel nicht benutzt, und mich auch sonst keiner unerlaubten Hilfsmittel bedient habe.

Ich erkläre, dass ich die Richtlinien des Senats der Montanuniversität Leoben zu "Gute wissenschaftliche Praxis" gelesen, verstanden und befolgt habe.

Weiters erkläre ich, dass die elektronische und gedruckte Version der eingereichten wissenschaftlichen Abschlussarbeit formal und inhaltlich identisch sind.

Datum 16.02.2023

Unterschrift Verfasser/in
Anna Margarethe Paulik

Acknowledgements

First of all, I would like to express my gratitude to Priv.-Doz. Mgr. David Holec PhD who was a great and very motivational supervisor for my thesis.

Furthermore, I want to thank Tomáš Záležák, Martin Friák and especially Antonín Dlouhý who not only provided me with valuable input and data for my thesis but also always made me feel included in their scientific dialogue.

Of course I also want to express my gratitude to any friends and family members who took the time to read my thesis and gave me valuable feedback, as well as all of my colleagues from the CMS group for our great inspirational discussions.

Lastly, I want to acknowledge the funding from OeAD which allowed me to travel to Brno to hold a presentation at the MSMF10 conference, as well as the “WKO Research Scholarship” and the “Wissenschaftspreis für Montanistinnen” which were a great honor for me to receive.

Contents

1	Introduction	1
2	Theory	3
2.1	Density Functional Theory (DFT)	3
2.1.1	The VASP code for DFT calculations	6
2.1.2	Calculation setup and Input files	7
2.2	The shape memory effect	11
2.2.1	Application and history of SMAs	14
2.3	Properties of NiTi	15
2.4	Hydride phases in NiTi	17
2.4.1	Lattice diffraction of NiTi Hydride phases	18
2.4.2	Hydrogen embrittlement	19
3	Implementation	20
3.1	Generation of different starting configurations	20
3.1.1	Random hydrogen placement	22
3.1.2	Hydrogen placement in nickel-planes	24
3.1.3	Hydrogen placement in titanium-planes	25
3.1.4	Hydrogen distributed between Ni- and Ti-planes	25
3.1.5	Hydrogen placement in the first octant of the supercell	26
3.2	Evaluation of the energetic stability	28
3.2.1	Formation energy	28
3.2.2	Mixing enthalpy	29
3.3	Evaluation of the energetic stability of geometrically confined cells	29
3.4	Evaluation of the equilibrium lattice parameters of partially confined cells	30
3.5	Evaluation of hydrogen distribution	31
3.6	Evaluation of mechanical stability	31
3.6.1	The stress-strain method	32

4	Determination of phase stability	34
4.1	Energy per atom for fully relaxed cells	34
4.1.1	Random hydrogen placement	34
4.1.2	Hydrogen placement in nickel planes	35
4.1.3	Hydrogen placement in titanium planes	36
4.1.4	Hydrogen placement in both nickel and titanium planes	36
4.1.5	Clustered hydrogen configuration	37
4.2	Energy per atom for confined cells	38
4.2.1	Relationship between energy per atom and cell shape	39
4.3	Correlation of energy with hydrogen distribution	40
4.4	Elastic constants of relaxed cells	46
4.5	Discussion of criteria for phase stability	50
5	Simulation of confined unit cells	52
5.1	Equilibrium lattice parameters of partially confined cells	52
5.1.1	Dependence on a general scaling parameter	52
5.1.2	Individually fitted lattice parameters	55
5.2	Phase change upon scaling confined cells	56
5.2.1	Possible explanation for the change in stresses	60
6	Discussion of diffraction patterns	62
6.1	Effect of hydrogen distribution on diffraction patterns	62
6.1.1	Comparison of diffraction patterns	63
6.1.2	Summary of observations	67
7	Closing remarks and outlook	68
7.1	Closing remarks	68
7.2	Outlook	69
.1	Python scripts	74
.2	Calculation parameters	74
.2.1	For atomic fcc nickel	74
.2.2	For atomic hcp titanium	75
.2.3	For molecular hydrogen	75
.3	Elastic tensors	75

List of Figures

1.1	Stent with guiding wire (figure taken from [3] under the CC BY-SA 4.0 licence).	2
2.1	Electronic relaxation steps. Using a starting electron density, the potentials are calculated. The Kohn-Sham equation is solved and a new density is calculated. These steps are then repeated with the new density until convergence is reached [9].	5
2.2	k -points using the “automatic” setting over cutoff energy; teal colored regions represent optimal convergence of the calculation with the desired accuracy of ± 1 meV/at.	8
2.3	Stress and temperature region where shape memory effects and pseudoelasticity/superelasticity are triggered [20]; Above M_d , no shape memory effects occur.	11
2.4	Stress-strain-diagram of a pseudoelastic material showing the hysteresis loop of the phase transformation [21].	12
2.5	One-way shape memory effect (figure taken from [22] under the CC BY-SA 4.0 licence).	13
2.6	Phase diagram of the binary nickel-titanium system (figure taken from [27] under the CC BY-SA 3.0 licence).	15
2.7	M_s temperature of NiTi phase for varying nickel content (figure taken from [28] under the public domain).	16
2.8	B2 austenite phase of NiTi.	16
2.9	B19' martensite phase of NiTi.	17
2.10	Possible interstitial positions for hydrogen in austenitic NiTi, A and C representing octahedral voids with different atomic configurations, B representing the tetrahedral void surrounded by two Ni and two Ti atoms (figure taken with permission from [31]).	18

2.11	Possible equilibrium positions of hydrogen; (a) position in the center of the tetrahedral void; (b) slightly off-center position in the octahedral void; (c) position in the center of the octahedral void (figure taken with permission from [31]).	18
2.12	Diffraction pattern including spots of the B2 phase (marked with red arrows) and of only the hydride phase (marked with blue arrows); courtesy to A. Dlouhý.	19
3.1	Orthorhombic unit cell; nickel atoms displayed in grey; titanium atoms displayed in blue.	20
3.2	Tetrahedral voids in the B2 structure (nickel atoms displayed in grey, titanium atoms displayed in blue and voids filled with light pink hydrogen atoms). Periodic images of atoms on the faces of the cell are included.	22
3.3	Tetrahedral voids in the orthorhombic structure; basal planes of the B2 cell displayed in green, blue and pink; hydrogen colored differently based on the corresponding basal plane.	22
3.4	Configuration of $\text{Ni}_{12}\text{Ti}_{12}\text{H}_{12}$ with hydrogen atoms placed in random tetrahedral voids (titanium atoms displayed in blue, nickel atoms displayed in grey and hydrogen displayed in light pink).	23
3.5	Starting configuration with hydrogen placed exclusively into the same lattice planes as nickel atoms (titanium atoms displayed in blue, nickel atoms displayed in grey and hydrogen displayed in light pink).	24
3.6	Translational vector between positions in nickel- and titanium planes (nickel atoms displayed in grey, titanium atoms displayed in blue).	26
3.7	Unit cell with hydrogen only in the first octant.	27
3.8	STEM-image of hydride phase precipitates in B2-NiTi matrix (marked with red lines); courtesy to A. Dlouhý.	30
3.9	Different strategies for quantifying the hydrogen distribution. Green, red and blue atoms schematically represent hydrogen, nickel and titanium atoms respectively.	31
4.1	(Left) formation energy/(right) mixing enthalpy against number of randomly distributed hydrogen atoms in the cell.	34
4.2	(Left) formation energy/(right) mixing enthalpy against number of hydrogen atoms in or mostly in Ni planes.	35
4.3	(Left) formation energy/(right) mixing enthalpy against number of hydrogen atoms in or mostly in Ti planes.	36

4.4	(Left) formation energy/(right) mixing enthalpy against number of hydrogen atoms distributed between Ni and Ti planes.	36
4.5	(Left) formation energy/(right) mixing enthalpy against number of clustered hydrogen atoms in the cell.	37
4.6	Formation energy for different starting configurations after partial relaxation.	38
4.7	Fully relaxed Ni ₁₂ Ti ₁₂ H ₁₂ with H mostly in Ni planes.	41
4.8	Minimal distances between different atom types for fully relaxed Ni ₁₂ Ti ₁₂ H ₁₂ with H mostly in Ni planes.	41
4.9	Fully relaxed Ni ₁₂ Ti ₁₂ H ₁₂ with H mostly in Ti planes.	42
4.10	Minimal distances between different atom types for fully relaxed Ni ₁₂ Ti ₁₂ H ₁₂ with H mostly in Ti planes.	42
4.11	Fully relaxed Ni ₁₂ Ti ₁₂ H ₁₂ with a clustered starting configuration. . . .	43
4.12	Minimal distances between different atom types for fully relaxed Ni ₁₂ Ti ₁₂ H ₁₂ with a clustered starting configuration.	43
4.13	Fully relaxed Ni ₁₂ Ti ₁₂ H ₂ with a clustered starting configuration with bonds to the closest Ti-atoms displayed.	44
4.14	Fully relaxed Ni ₁₂ Ti ₁₂ H ₂ with a starting configuration in nickel planes with bonds to the closest Ti-atoms displayed.	45
4.15	Random starting configuration for Ni ₁₂ Ti ₁₂ H ₁₆ (left) and fully relaxed Ni ₁₂ Ti ₁₂ H ₁₆ with bonds to the closest Ni-atoms displayed (right). . .	45
4.16	Visualized Young's modulus of the B2 phase.	48
4.17	Visualized Young's modulus of the fully relaxed hydride with H mostly in Ti planes.	48
4.18	Visualized Young's modulus of the partially relaxed hydride with H mostly in Ti planes.	49
4.19	Visualized Young's modulus of the partially relaxed hydride with H mostly in Ni planes.	49
5.1	Energy per atom for a coarse fit up to a 10% length increase (left) and values at 0.1% intervals around the minimum at 2.5% (right). . .	53
5.2	Magnitude of highest normal stress (evaluated for each data point, so it is not always the same stress component) for a coarse fit up to a 10% length increase (left) and values at 0.1% intervals around the minimum at 2.5% (right).	53
5.3	Normal stresses for different cell sizes.	53

5.4	Shear components of the stress tensor over the scaling parameter for the coarse fit up to a 10% length increase (left) and values at 0.1% intervals around the minimum at 2.5% (right).	54
5.5	Shear stress component τ_{bc} over the scaling parameter for lattice parameter, showing abrupt changes in stresses for certain cell sizes (area of interest marked in green).	56
5.6	Comparison of relaxed structures for an increase of lattice parameters of 5.525% (dark colors) and 5.535% (light colors).	57
5.7	Comparison of relaxed structures for an increase of lattice parameters of 5.535% (dark colors) and 5.550% (light colors).	57
5.8	Comparison of relaxed structures for an increase of lattice parameters of 5.550% (dark colors) and 7.50% (light colors).	58
5.9	Comparison of relaxed structures for an increase of lattice parameters of 5.535% (dark colors) and 6.750% (green and brown atoms).	59
5.10	Energies per atom for all relaxed structures.	60
5.11	Energies per atom for all relaxed structures.	61
6.1	Diffraction pattern of the B2 matrix.	63
6.2	Diffraction pattern of the unrelaxed structure with hydrogen placed in tetrahedral voids.	64
6.3	Diffraction pattern of the unrelaxed structure with hydrogen placed in tetrahedral voids; detection threshold 10^{-4} times smaller than in figure 6.1.	64
6.4	Diffraction pattern of the completely relaxed structure.	65
6.5	Diffraction pattern of the relaxed structure with fixed cell shape and size.	66
6.6	(a) Diffraction pattern of the fully relaxed structure with hydrogen atoms (also shown in figure 6.4); (b) diffraction pattern of the fully relaxed structure with hydrogen atoms removed.	67

List of Tables

2.1	Different relaxation modes defined by the “ISIF”-tag.	9
2.2	Pseudopotentials used for each element.	10
3.1	Fractional coordinates of nickel and titanium atoms in the orthorhombic unit cell	21
3.2	Fractional coordinates of twelve randomly chosen tetrahedral voids filled with hydrogen atoms.	23
3.3	Relative coordinates of hydrogen atoms in Ni-planes.	24
3.4	Relative coordinates of hydrogen atoms in Ni or Ti-planes.	26
3.5	Relative coordinates of hydrogen atoms for a configuration with clustered hydrogen atoms.	27
3.6	Chemical potentials of elements in $\text{Ni}_{12}\text{Ti}_{12}\text{H}_x$ in their most stable state.	28
4.1	Energy per atom and monoclinic angles for different structures of $\text{Ni}_{12}\text{Ti}_{12}\text{H}_{12}$ after relaxation.	39
4.2	Minimum and maximum shear moduli, Young’s moduli and Poisson’s ratios for the B2 phase [30]	46
4.3	Minimum and maximum Young’s moduli, shear moduli and Poisson’s ratios for the most energetically stable hydrogen configuration when fully relaxed.	46
4.4	Minimum and maximum Young’s moduli, shear moduli and Poisson’s ratios for the most energetically stable hydrogen configuration with only atomic positions relaxed.	47
4.5	Minimum and maximum Young’s moduli, shear moduli and Poisson’s ratios for a less energetically stable hydrogen configuration with only atomic positions relaxed.	47
4.6	Comparison of average bulk modulus, Young’s modulus, shear modulus and Poisson’s ratio calculated using the Voigt scheme for the different configurations.	47

5.1 Initial (unrelaxed) lattice parameters and their corresponding scaled
equilibrium lattice parameters. 55

Nomenclature

NiTi	Intermetallic phase of nickel and titanium; also commonly known as "Nitinol"
hydride	Intermetallic phase where hydrogen is one of the constituents
SMA	Shape Memory Alloy
DFT	Density Functional Theory
\hat{H}	Hamiltonian operator
\hat{H}_{KS}	Hamiltonian operator for a fictitious system of non-interacting particles based in the Kohn-Sham approach
h	Planck constant
m_e	Electron mass
\hat{V}	Potential energy operator
n	Electron density
ε_{XC}	Exchange-correlation energy density
LDA	Local Density Approximation
GGA	Generalized Gradient Approximation
VASP	Vienna ab-initio simulation package
k -points	Sampling points in the first Brillouin zone
austenite	High temperature, high symmetry phase of NiTi (B2)
martensite	Low temperature, low symmetry phase of NiTi (B19')
twinning	Diffusion-less lattice deformation from a high-symmetry to a low-symmetry phase

BCC	Body centered cubic
FCC	Face centered cubic
HCP	Hexagonal close-packed
B2-phase	High temperature austenite phase of NiTi with a BCC unit cell
B19'-phase	Low temperature martensite phase of NiTi with a monoclinic unit cell
monoclinic	Unit cell with three different lattice parameters and two right lattice angles
orthorhombic	Unit cell with three different lattice parameters and three right lattice angles
octahedral void	Interstitial space in a unit cell which is surrounded by six equidistant lattice atoms
tetrahedral void	Interstitial space in a unit cell which is surrounded by four equidistant lattice atoms
$\varepsilon_F^{\text{Ni}_{12}\text{Ti}_{12}\text{H}_x}$	Formation energy per atom for a hydride phase with a composition of $\text{Ni}_{12}\text{Ti}_{12}\text{H}_x$
μ	Chemical potential
$\varepsilon_{mix}^{\text{Ni}_{12}\text{Ti}_{12}\text{H}_x}$	Mixing enthalpy per atom for a hydride phase with a composition of $\text{Ni}_{12}\text{Ti}_{12}\text{H}_x$
STEM	Scanning transmission electron microscope
ELATE	Tool for analyzing and visually displaying elastic tensors
VESTA	Tool for constructing and displaying unit cells

Chapter 1

Introduction

The equiatomic alloy of Nickel and Titanium, NiTi, is an important material for “smart” applications due to its so-called shape memory effect. There are three different mechanisms which facilitate the shape memory effect: (1) the reversible straining of a material well beyond its expected yield-point (pseudoelasticity), (2) undoing a complex plastic deformation through heating of the material (one-way effect) and (3) a change between two phases with macroscopically different shapes through temperature changes (two-way effect). The mechanisms facilitating the shape memory effect will be further explored in chapter 2.2.

These effects can be utilized in a plethora of different applications, most notably and importantly in the medical field, but also many everyday-life products. Pseudoelastic eyeglass-frames, for example, provide not only the advantage that they are foldable without the need for joints, but they are also more comfortable for the wearer since they are aligning themselves to better fit the person’s individual face shape and equalize the applied pressure [1].

In medical applications, shape memory alloys (SMAs), combined with advanced imaging techniques, have been an enabling technology for modern minimally invasive surgery methods. Implants such as stents (see figure 1.1), which are thin wire tubes that can keep arteries open, are commonly made from SMAs, specifically Nitinol, since this mechanism allows for them to be inserted in a very small, folded-up state via a small incision, which is only possible due to the pseudoelastic effect [2].

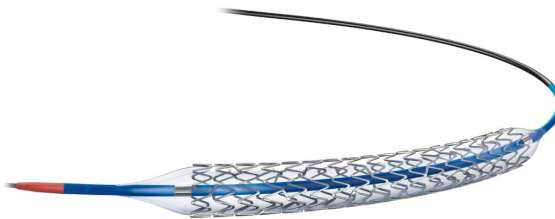


Figure 1.1: Stent with guiding wire (figure taken from [3] under the CC BY-SA 4.0 licence).

The extensive use of NiTi has first started in the 1990s and while a lot of research has been done on the properties of this material and the shape memory effect, there is still a lot left to be explored and understood [4]. Some very recent examples of published research are on the mechanical behavior of Nitinol stents are Ref. [5, 6, 7]. For biocompatibility, the interactions of NiTi with other elements and the possible formation of intermetallic ternary phases can be very critical. A particularly important question is, what happens when NiTi is exposed to a hydrogen-rich environment. Specifically NiTi implants are permanently in a close contact with bodily fluids and tissues which only very rarely exhibit pH of exactly 7 and thus usually contain free H^+ or OH^- ions. Thereby, they may form new ternary phases with NiTi. In previous experimental research by Dlouhý and coworkers, it has been found that hydrogen diffuses into the specimen and potentially forms a new intermetallic hydride phase. The NiTi sample was charged with hydrogen and then examined using scanning transmission electron microscope (STEM) imaging.

This work aims to further characterize the proposed hydride phase in terms of its equilibrium cell shape, the atomic fraction and position of hydrogen atoms in the unit cell, as well as general energetic and mechanical stability. This is achieved through atomistic simulation, precisely the method of Density Functional Theory (DFT) and the VASP code (which will be further described in chapter 2.1). The main purpose of these simulations is to supplement the experimental findings with data at a scale, which would not be accessible through experiments alone (such as the most stable positions of hydrogen in the cell).

Chapter 2

Theory

2.1 Density Functional Theory (DFT)

Density Functional Theory is a so called “first principle” or “ab initio” method of simulation. The defining characteristic of ab initio methods is, that no specific interatomic potentials have to be fitted and all the necessary information about atomic interactions can be inferred directly from the basic laws of physics. DFT connects the classical approach of the Newtonian mechanics, forces acting on masses, with the quantum mechanical approach using wave functions to describe electronic states. The relaxation of a structure into its ground state is performed through alternating electronic and ionic relaxation steps. During an electronic relaxation step, the wave function corresponding to the ground state of the electronic subsystem is calculated for fixed positions of atomic nuclei. This is followed by an ionic relaxation step, during which atomic nuclei are moved in the direction of the calculated residual forces obtained from the last electronic step.

The separation of the movement of electrons and nuclei is based on the Born-Oppenheimer approximation. It states, that due to the drastic difference in mass between electrons and nuclei, if the same force is acting on an electron and a nucleus, the resulting movement of the two different types of particles occurs at vastly different time scales. During the time that it takes an electron to move, the change in position of the nucleus is negligible, which means that nuclei can be seen as stationary during electronic relaxation steps. During electronic relaxation steps, nuclei are only included in the calculation in a form of a potential landscape acting on the electrons.

The state of a system is described by the many-body wave function. The corresponding Schrödinger equation is very complex, even when just a relatively small number of particles is considered. In DFT, the many-body wave function is replaced by an electron density which results in a single-particle problem. The electron density, n , is defined as the probability of finding N electrons at a certain position \mathbf{r} [8].

The justification for why each wave function is uniquely correlated with a distinct electron density is provided by the two theorems of Hohenberg and Kohn [8, 9]. The first theorem says that if two systems of electrons are trapped in two potentials, $V_1(\mathbf{r})$ and $V_2(\mathbf{r})$, but have the same ground state density, then $V_1(\mathbf{r}) - V_2(\mathbf{r}) = \text{const.}$ The fact that the energy landscape only differs by an additional constant potential leads to the conclusion, that the ground state electron density uniquely determines the potential, except for an additive constant. This means that the potential is a unique functional of the electron density (up to the additive constant). Consequently, the Hamiltonian must also be a unique functional of the electron density. The second theorem of Hohenberg and Kohn states that the variational principle can be used to determine the ground state density, which is the electron density that minimizes the total energy of the system corresponds to the ground state.

While the variational principle can theoretically be used to calculate the ground state density, it is usually not very practical, because the interaction between electrons makes the system of equations non-linear. The “Kohn-Sham approach” proposes to replace the system of interacting particles with a system of fictitious non-interacting particles, which corresponds to the same electron density but has no direct physical meaning. This results in a set of linear equations which significantly reduces the computational load [8].

The Schrödinger equation for the many electron problem (equation 2.1) gets replaced by the Kohn-Sham equation (equation 2.3).

$$\hat{H}\Psi = E\Psi \tag{2.1}$$

with

$$\hat{H} = -\frac{\hbar^2}{2m_e}\nabla^2 + \hat{V}_{e-e} + \hat{V}_{ext} \tag{2.2}$$

$-\frac{\hbar^2}{2m_e}\nabla^2$... kinetic energy operator (\hat{T}_0)

\hat{V}_{e-e} ... potential operator of electron-electron interaction

\hat{V}_{ext} ... external potential operator of atomic nuclei

$$\hat{H}_{KS}\Psi = E\Psi \quad (2.3)$$

$$\hat{H}_{KS} = -\frac{\hbar^2}{2m_e}\nabla^2 + \frac{e^2}{4\pi\epsilon_0} \int \frac{n(\mathbf{r}')}{|\mathbf{r}' - \mathbf{r}|} d\mathbf{r}' + \hat{V}_{ext} + \hat{V}_{XC} \quad (2.4)$$

$\frac{e^2}{4\pi\epsilon_0} \int \frac{n(\mathbf{r}')}{|\mathbf{r}' - \mathbf{r}|} d\mathbf{r}'$... Hartree potential operator (\hat{V}_H)

\hat{V}_{XC} ... exchange-correlation potential operator

The exchange-correlation potential (V_{XC}) describes the interaction between electrons which is missing from the system since the particles described by the Kohn-Sham equation are non-interacting. This potential cannot be calculated analytically and must be approximated as described in section 2.1.

The principle of electronic relaxation steps in DFT, using the Kohn-Sham equation and an estimate for V_{XC} , is schematically shown in figure 2.1.

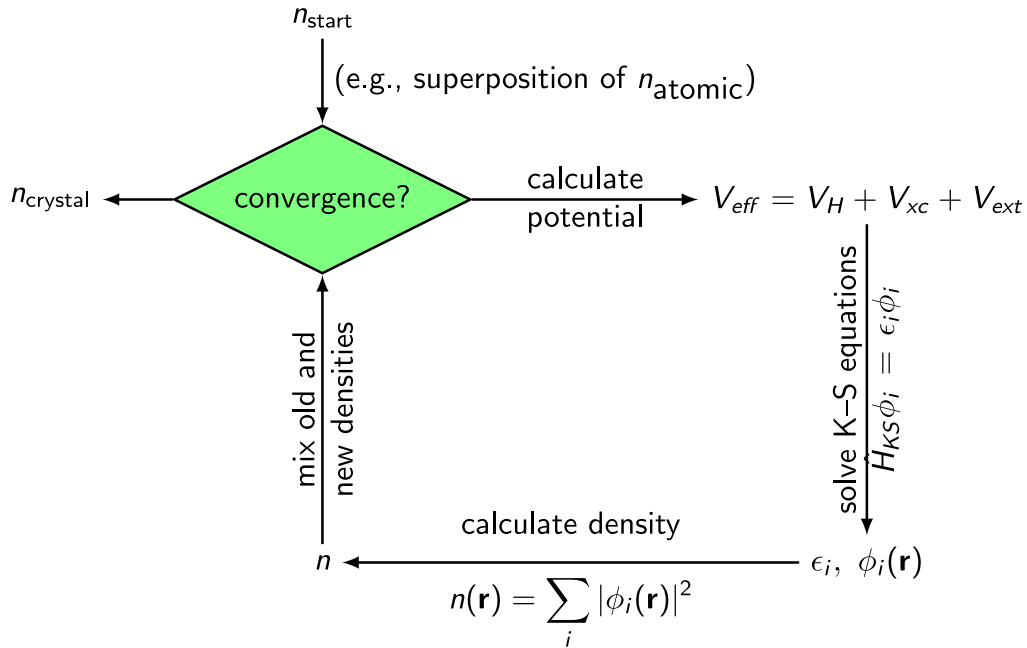


Figure 2.1: Electronic relaxation steps. Using a starting electron density, the potentials are calculated. The Kohn-Sham equation is solved and a new density is calculated. These steps are then repeated with the new density until convergence is reached [9].

Estimating the exchange-correlation potential

As already mentioned in the previous section, in order to calculate the exchange-correlation potential, an approximation has to be made. One strategy used to estimate the exchange-correlation potential is the Local Density Approximation (LDA). It is assumed that the exchange-correlation energy density ε_{XC} depends only on the local electron density [8]. The resulting exchange-correlation functional is described by equation 2.3:

$$V_{XC}^{LDA}[n(\mathbf{r})] = \int n(\mathbf{r})\varepsilon_{XC}^{LDA}(n(\mathbf{r}))d\mathbf{r} \quad (2.5)$$

Another approach for estimating the exchange-correlation potential is the Generalised Gradient Approximation (GGA), described by equation 2.4. In this case, not only the local electron density, but also its first derivative influence the exchange correlation energy density ε_{XC} :

$$V_{XC}^{GGA}[n(\mathbf{r})] = \int n(\mathbf{r})\varepsilon_{XC}^{GGA}(n(\mathbf{r}), \nabla n(\mathbf{r}))d\mathbf{r} \quad (2.6)$$

2.1.1 The VASP code for DFT calculations

“VASP” is an abbreviation which stands for “Vienna ab-initio simulation package”, a code which allows for ab-initio modelling of systems on the atomic scale. For this work the GGA approach described in the previous section has been used to calculate the exchange-correlation potential. Section 2.1.2 explains how calculations are set up in VASP and which parameters are necessary.

***k*-points**

k-points describe the sampled points in the first Brillouin zone of the reciprocal lattice and create the mesh for the DFT simulation. The transformation of a real space integral to a reciprocal space mesh is essentially a Fourier transformation. The integral in real space is transformed to a reciprocal space summation, which can be solved as an eigenvalue problem. A higher number of *k*-points used corresponds to a higher accuracy, but also a bigger computational load [10].

cutoff-energy

Solutions for the Kohn-Sham equation can be found using Bloch’s theorem, which says that if the potential is periodic, the solutions can be written as a plane wave multiplied with a lattice-periodic function. Fourier expansion then leads to an in-

finite sum of functions that depend on just one reciprocal lattice vector each. To restrict this infinite set of equations, an energy cutoff (which directly corresponds to a certain maximum reciprocal lattice vector) is chosen, where the expansion is truncated. This parameter is usually chosen through a convergence test (see chapter 3.1.1) so that the calculation reaches the desired accuracy while demanding as little resources as possible.

2.1.2 Calculation setup and Input files

In the following, the practical setup and determination of necessary parameters for the VASP calculations used for this work are discussed. To set up calculations using the VASP code, several input files must be provided in order to define the unit cell, the types, numbers and positions of atoms, the pseudopotentials, the number and distribution of k -points, the cutoff energy, the maximum number of relaxation steps, as well as other properties relating to, for example, magnetism and spins [11, 12, 13, 14].

Convergence test

Two important parameters, which have to be included, are the number of k -points and the cutoff energy. In order to find the optimal combination that provides the required accuracy at minimal computational effort, a convergence test is performed; the cell is electronically relaxed (ISIF = 0; see the following section) using a set of possible combinations of the two parameters. The energy differences between the last two relaxation steps before truncation are compared to find the threshold of convergence.

Figure 2.2 shows the results from the convergence test for the B2-structure (see section 2.3 for an explanation of the different possible structures of NiTi). When using the “automatic” distribution of k -points, the exact number of k -points in each direction of the reciprocal space can be found in the output files. For all further performed calculations using the orthorhombic unit cell, 55 automatic k -points — which corresponds to a mesh of $6 \times 7 \times 11$ k -points for the orthorhombic cell — and a cutoff energy of 500 eV have been used. This combination is well within the area of convergence, defined by the teal colored areas in figure 2.2.

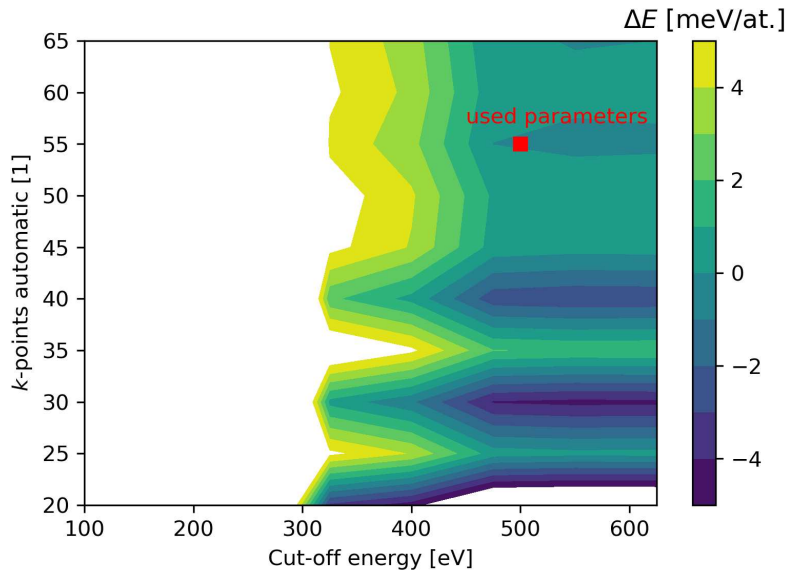


Figure 2.2: k -points using the “automatic” setting over cutoff energy; teal colored regions represent optimal convergence of the calculation with the desired accuracy of ± 1 meV/at.

As implied in the previous paragraph, the results from the convergence test of the B2 structure also gives the parameters for the relaxation of orthorhombic structures with differing amounts of hydrogen. This way the computational effort is minimised, since the B2 structure contains only one nickel and one titanium atom as opposed to twelve of each in the orthorhombic unit cell. The simplification is justified by the fact, that the unit cell of the orthorhombic phase without hydrogen atoms exactly represents twelve B2 unit cells. The k -point density and the cutoff energy for these two configurations must thus be the same. The influence of hydrogen on the convergence is assumed to be negligible, since the number of k -points and the cutoff energy, which have been picked for the calculations are well within the area of convergence.

INCAR

The INCAR-file is a text file, which specifies different parameters of the calculation using “tags”. Important parameters for the relaxation of the hydride phase are “ENCUT” which specifies the cutoff energy in eV (determined by the convergence test), “NSW”, which defines the maximum number of ionic relaxation steps (the number of steps after which the calculation will automatically terminate in case ionic convergence has not been reached), and “ISIF” which defines different modes of relaxation. A list of the different modes can be found in table 2.1.

Table 2.1: Different relaxation modes defined by the “ISIF”-tag.

ISIF	relaxation of cell size	of cell shape	of atom positions
0	no	no	no
2	no	no	yes
3	yes	yes	yes
4	no	yes	yes
5	no	yes	no
6	yes	yes	no

In the following, an exemplary INCAR file with the appropriate tags for a full relaxation of NiTiH (change in cell shape, cell size and atomic positions) is shown:

```

00  ENCUT = 500
01  IBRION = 2
02  ISIF = 3
03  ISYM = 0
04  LCHARG = False
05  LWAVE = False
06  NSW = 100

```

In the case shown, the cutoff energy is set to 500 eV, which is a result from the convergence test of B2 NiTi (see section 2.1.2). The IBRION-tag specifies the algorithm used for relaxation and has been set to 2, which corresponds to ionic relaxation with the conjugate gradient algorithm. This algorithm has been used for all following runs because it is relatively simple and sufficiently accurate. “ISIF = 3” defines that the cell shape, cell size and atomic positions are not fixed. With the ISYM-tag, symmetry can be enforced. Due to the highly asymmetric expected shape of the relaxed supercell, this feature has been turned off by setting the parameter to 0. If LCHARG and LWAVE are set to “true”, files containing the charge density and the wavefunction are written at the end of the run. Since these files are not necessary for the present evaluation, these features have been turned off. Lastly, the NSW-tag specifies that the run will terminate after 100 ionic relaxation steps if ionic convergence is not reached. In that case, the relaxation can be restarted with the new atomic positions from the final ionic step in order to continue the run.

POSCAR

The POSCAR-file determines the initial atomic positions, cell parameters and cell angles of the modelled structure. For this work, the cell has been created using VESTA (a program by JP-minerals for 3D visualizing of atomic structures [15]) in which the structures can be directly exported in the “.vasp”-format. The 3D visualization function has also been used to create images for the following chapters of this thesis.

An exemplary POSCAR-file for B2 NiTi is shown in the following:

```

01      NiTi
02      1.0
03          2.9930000305      0.0000000000      0.0000000000
04          0.0000000000      2.9930000305      0.0000000000
05          0.0000000000      0.0000000000      2.9930000305
06          Ni   Ti
07          1   1
08      Direct
09          0.0000000000      0.0000000000      0.0000000000
10          0.5000000000      0.5000000000      0.5000000000

```

Line 1 is the name of the structure and can be seen as a comment-line; line 2 is a scaling factor, which is used to scale all lattice constants up or down at the same time. In line 3-5, the lattice parameters are defined individually in Cartesian coordinates in the unit Ångström. Line 6 lists every type of atom in the unit cell with the respective number of atoms in line 7. From line 8, the relative positions of the atoms in the unit cell are listed (in the order used in lines 6 and 7).

POTCAR

The POTCAR-file includes the pseudo-potentials for each type of atom in the cell. For relaxation of the hydride, the pseudopotentials recommended by the VASP user guide have been used. The different potentials are listed in table 2.2[16].

Table 2.2: Pseudopotentials used for each element.

Element	potential
Ni	PAW_PBE Ni
Ti	PAW_PBE Ti_sv
H	PAW_PBE H

2.2 The shape memory effect

The description of the shape memory effect in this section is based on Ref. [17, 18, 19]. The shape memory effect is a phenomenon which occurs in certain alloys and is facilitated by phase transitions between a highly symmetrical, high temperature austenite phase and a lower symmetry, low temperature martensite phase. The defining characteristics of a martensitic transformation are, that it happens instantaneously and without diffusion, only through local twinning or shear deformation of the lattice. It is thus fully reversible. There are several types of shape memory effects, which a material can exhibit, depending on the temperature and applied stress. The regions where different effects occur are shown in figure 2.3.

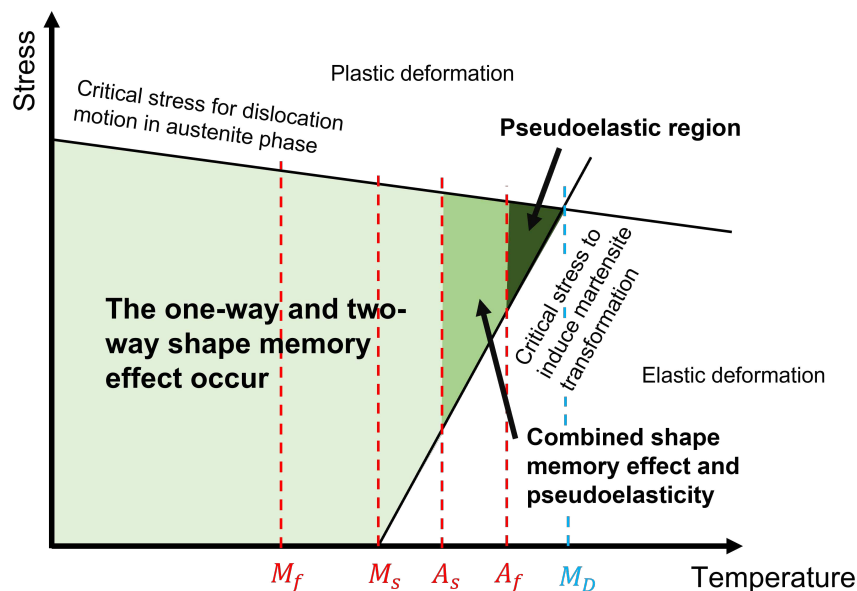


Figure 2.3: Stress and temperature region where shape memory effects and pseudoelasticity/superelasticity are triggered [20]; Above M_d , no shape memory effects occur.

Pseudoelasticity (often also called superelasticity) is an effect where the martensitic transformation is stress-induced. One condition, which has to be met in order for pseudoelasticity to occur, is that the austenite finish temperature (A_f) needs to be lower than the application temperature. This means that the unstrained material is in its austenite phase. Furthermore, the applied stress may only be between the required stress to induce martensitic transformation and the yield stress of the austenite phase (higher stress would result in irreversible plastic deformation, lower stresses do not trigger the pseudoelastic effect). The region in which pseudoelasticity is possible is shown in figure 2.3.

As shown in figure 2.4, a stress plateau is present in the stress-strain diagram when the critical stress is reached and the material undergoes a phase transition from austenite to detwinned martensite (in detwinned martensite, the monoclinic angle is always aligned in the same direction while it alternates for twinned martensite); the shape change due to detwinning accomodates further strains in the material beyond the linear elastic regime. After the transformation, the stress increases again with a slope corresponding to the Young's modulus of the martensite phase.

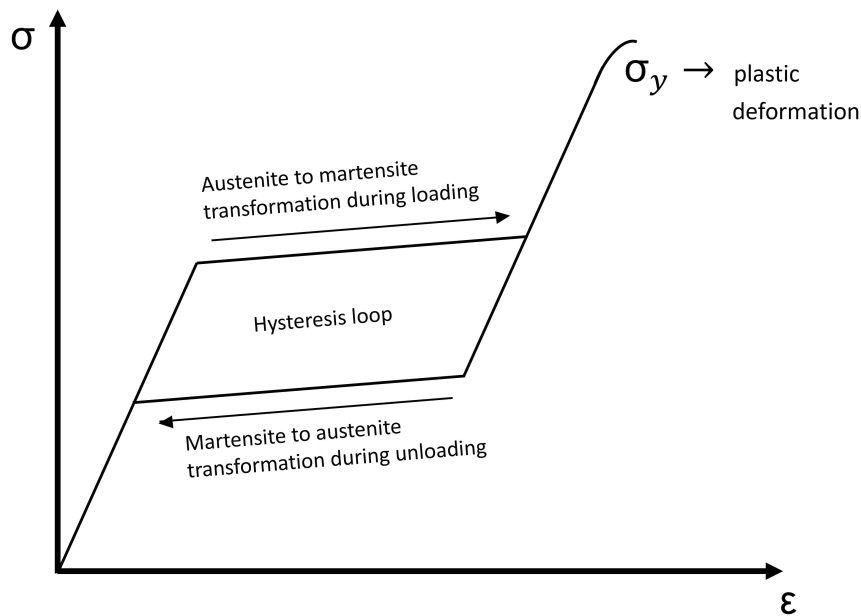


Figure 2.4: Stress-strain-diagram of a pseudoelastic material showing the hysteresis loop of the phase transformation [21].

During unloading, the inverse phase transition occurs, resulting in a plateau at lower stresses than during loading. The area inside this hysteresis-loop corresponds to the energy dissipated during the process.

The one-way effect utilizes thermally induced martensitic transformations to make the material “remember” a shape. For this effect to work, the temperature at which the austenite starts to form during heating (A_s) has to be above the application temperature of the material, but depending on the application, might be close to it so that the effect can be triggered by a small temperature increase. Figure 2.5 shows the working principle of the one-way-effect in the stress-strain-temperature-diagram.

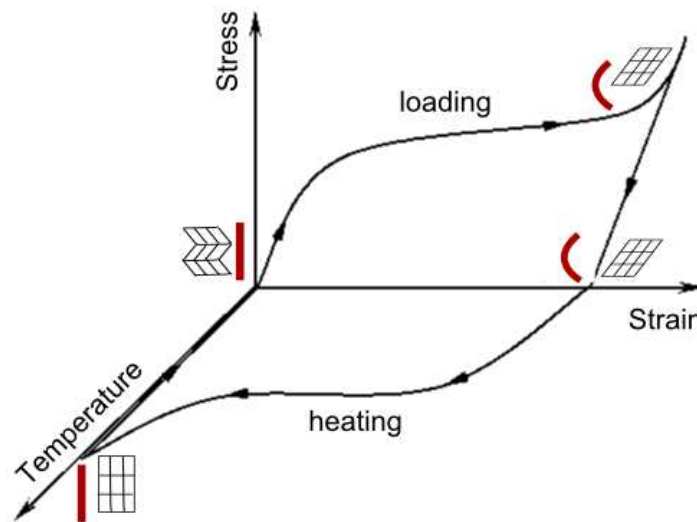


Figure 2.5: One-way shape memory effect (figure taken from [22] under the CC BY-SA 4.0 licence).

The material first gets heated above the austenite finish temperature (A_f), where the material has undergone a complete phase change from martensite to austenite, and is then mechanically formed into its desired shape. This step is followed by cooling of the material below the M_f temperature, the temperature where the whole material is in the martensite phase. The martensite forms diffusionless by twinning, since this type of deformation includes little movement of the atoms and leads to low internal stresses.

When the material gets strained beyond the elastic regime at this point, the first mode of accommodating the stresses is detwinning of the martensite. After unloading, the deformed structure of the detwinned martensite persists.

To recover the original shape, the material is heated again above the austenite finish temperature (A_f) and the phase transition from deformed martensite to austenite occurs. Since the movement of each atom between the twinned and detwinned state is minimal, the corresponding atomic configuration in the austenite phase is identical to the starting configuration, as long as no plastic deformation due to dislocation sliding has occurred. The material is now in its original shape and after cooling the material below M_f , the original twinned martensite structure is formed again.

The two-way effect distinguishes itself from the one-way-effect through the fact that the structural change occurs at constant stress and is triggered by heating and cooling of the material. It allows for reversible switching between two different configurations and requires prior “training” of the material. During “training”, the one-way effect is repeated under constant load in order to introduce lattice defects which stabilize the desired detwinned martensite structure. If the material is then cooled below M_f , the “trained” structure is formed which results in a shape change from the austenite phase. A caveat which limits the utility of the two-way effect is that during cooling, only very low external stresses may be present in order to reach the trained configuration. Otherwise, the initial untrained martensite would be formed.

2.2.1 Application and history of SMAs

One of the most important applications for the shape memory effect is in minimally invasive surgery (MIS), which, when compared to conventional open surgery, reduces complications, accelerates healing and thus also leads to shorter hospital stays. The MIS has been widely popularized in the 1990s and is now state of the art procedures, which are widely practiced. One particular example where tools made from Nitinol are used is in endoscopic surgery. The curved tools can be superelastically deformed to fit inside a straight tube for easy insertion into the body [4].

Another use of SMAs in medical science is for drug delivery systems, which allow for controlled administering of drugs inside the body. The applicable concepts range from coated stents over nanoporous Nitinol specimens to sophisticated systems with pumps, that can be activated through radio frequency heating [23, 24, 25]. Furthermore, the one-way-effect makes Nitinol a viable suture material, because it can be used for stitching and then revert back to its original state through heating [26].

Besides the aforementioned medical applications, SMAs are being used in micro- and nanomechanical system (MEMS/NEMS). Furthermore, SMAs have a plethora of potential applications in daily life. One example is using a pseudoelastic material for eyeglass frames to make them foldable without joints (see figure 1.1a))[4].

2.3 Properties of NiTi

Nickel-titanium alloys, also known as Nitinol, are widely used in medical applications, mainly due to their superior biocompatibility and low toxicity. The nickel-titanium phase diagram showing all of the intermetallic phases in the system is depicted in figure 2.6. The SMA NiTi-phase specifically forms between a nickel-concentration of around 50 to 55 at.% and has a melting point of 1310 °C.

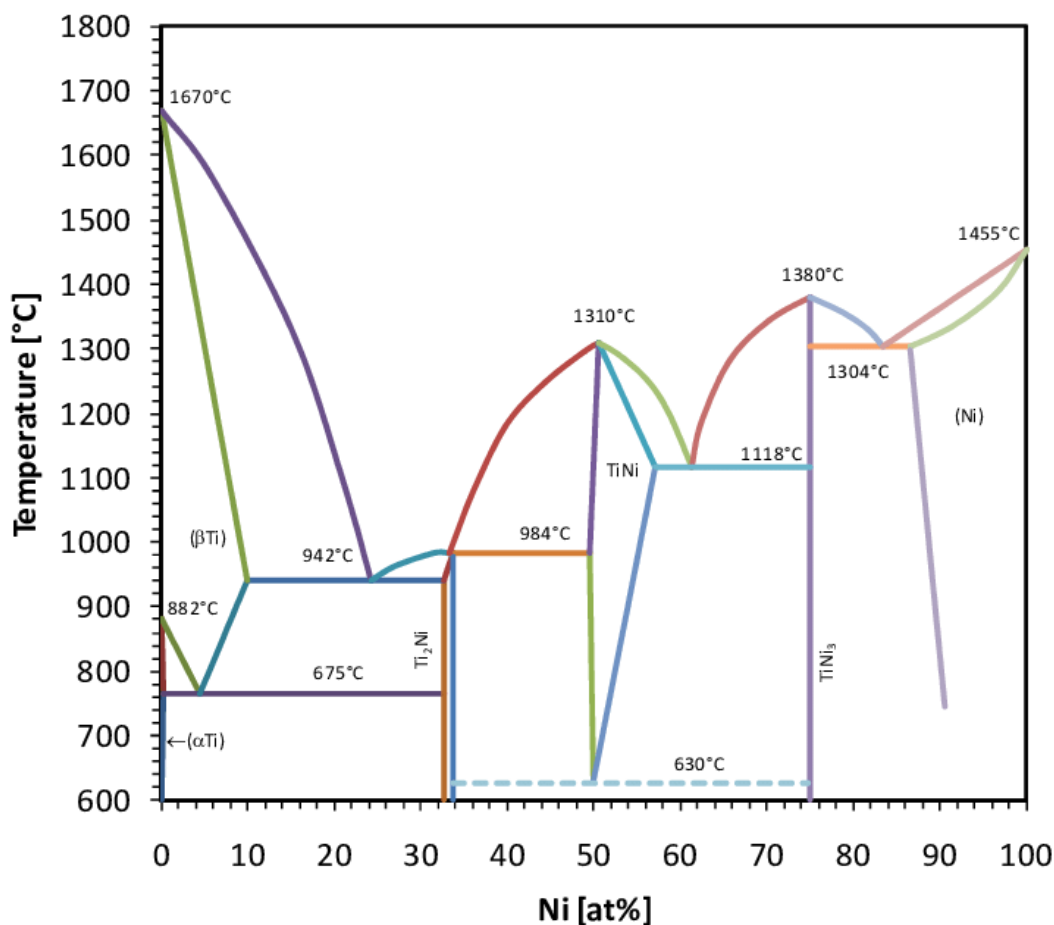


Figure 2.6: Phase diagram of the binary nickel-titanium system (figure taken from [27] under the CC BY-SA 3.0 licence).

In the NiTi-phase, the one-way or two-way shape memory effects, as well as superelasticity are possible, depending on the atomic fractions of Ni and Ti. Figure 2.7 shows the dependence of the martensite start temperature on nickel content within the NiTi phase field. [17, 19]

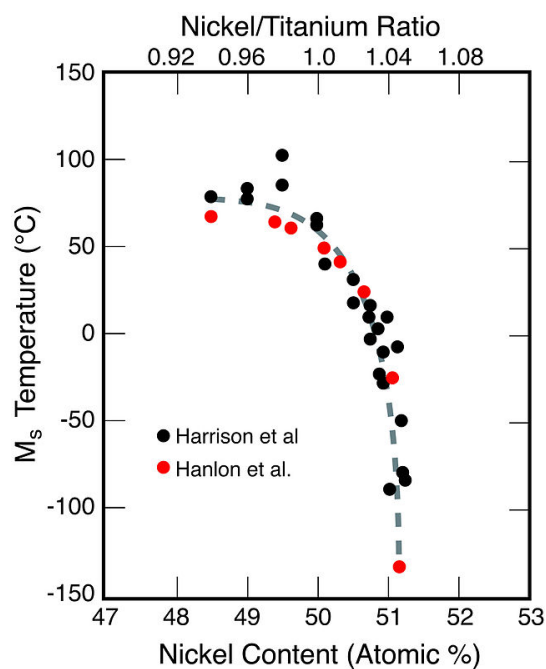


Figure 2.7: M_s temperature of NiTi phase for varying nickel content (figure taken from [28] under the public domain).

The austenite phase of NiTi, shown in figure 2.8 is also called the B2-phase and has the CsCl, body-centered cubic crystal structure with a lattice parameter of 2.993 \AA . It belongs to the $m\bar{3}m$ point group. The density of the phase is 6.60 g cm^{-3} and the formation energy per atom is -0.348 eV [29, 30].

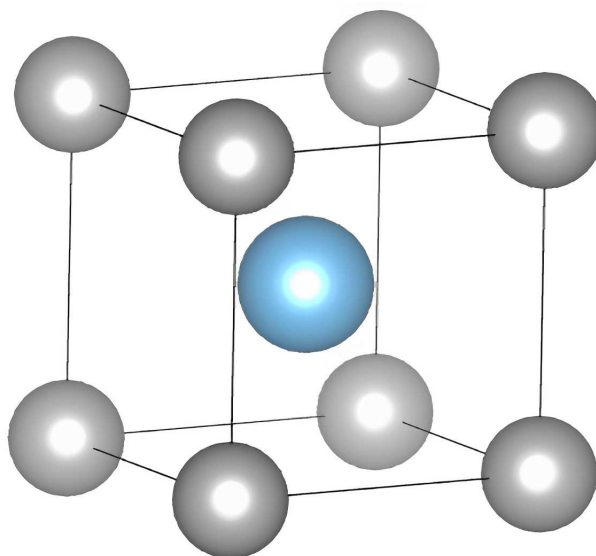


Figure 2.8: B2 austenite phase of NiTi.

The martensite phase formed by cooling the B2 austenite structure is also called the B19'-phase. It has a monoclinic structure with the lattice parameters $a = 4.055 \text{ \AA}$, $b = 2.915 \text{ \AA}$ and $c = 4.754 \text{ \AA}$ and a monoclinic angle of $\alpha = 79.068^\circ$. The density is 6.41 g cm^{-3} , slightly lower than for the austenitic phase and the formation energy is -0.396 eV . The phase belongs to the $2/m$ point group. Figure 2.9 depicts the B19' martensite phase [30].

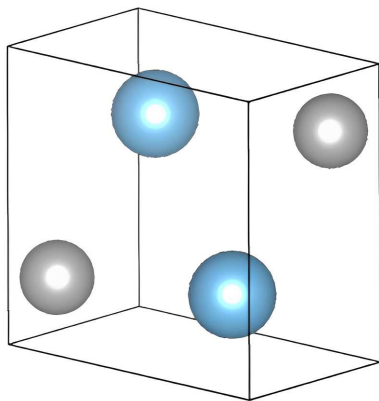


Figure 2.9: B19' martensite phase of NiTi.

2.4 Hydride phases in NiTi

The experimental research of the effects that environmental hydrogen has on NiTi and the theoretical examination of the effects using atomistic modelling is an ongoing process. Results from internal friction experiments suggest that hydrogen at a concentration above 4.5 at.% has an influence on the martensitic transformation, inhibiting the shape memory effect. This result has been confirmed by further testing, as well as ab initio DFT simulations [31, 32].

A topic of ongoing research is which atomic sites are occupied by interstitial hydrogen. Using DFT calculations, the ground state energy for different positions of interstitial hydrogen in the cell has been determined by Holec et. al [31]. The different sites are shown in figure 2.10. It was concluded that octahedral voids surrounded by four titanium atoms and two nickel atoms (position C) yield the lowest energy state. It has also been found, that with increasing hydrogen content, the energy difference between the martensite phase and the austenite phase diminishes, which suggests that interstitial hydrogen might stabilize the B2 phase at lower temperatures.

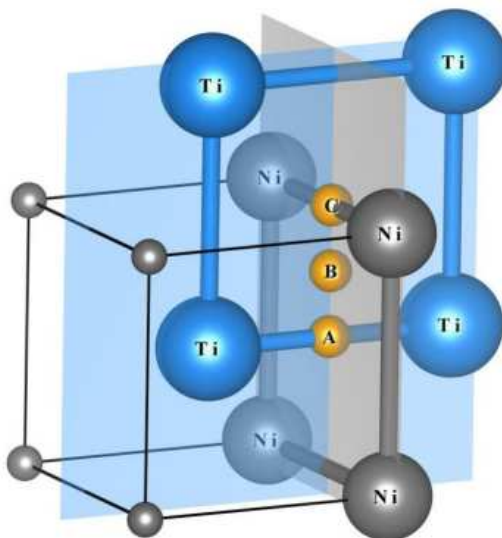


Figure 2.10: Possible interstitial positions for hydrogen in austenitic NiTi, A and C representing octahedral voids with different atomic configurations, B representing the tetrahedral void surrounded by two Ni and two Ti atoms (figure taken with permission from [31]).

The results of the structural relaxations show, however, that hydrogen atoms do not sit in the center of the octahedral voids, but are slightly displaced as shown in figure 2.11 (b).

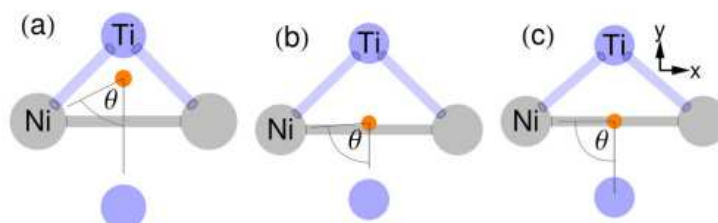


Figure 2.11: Possible equilibrium positions of hydrogen; (a) position in the center of the tetrahedral void; (b) slightly off-center position in the octahedral void; (c) position in the center of the octahedral void (figure taken with permission from [31]).

2.4.1 Lattice diffraction of NiTi Hydride phases

It has been reported by Dlouhý and colleagues, that the lattice diffraction pattern of hydrogen-charged B2 NiTi significantly differs from the diffraction pattern of pure B2 NiTi. The resulting pattern shown in figure 2.12 suggests that a hydride phase with an orthorhombic unit cell is formed. This structure will be used in the following chapters as a starting point for DFT calculations.

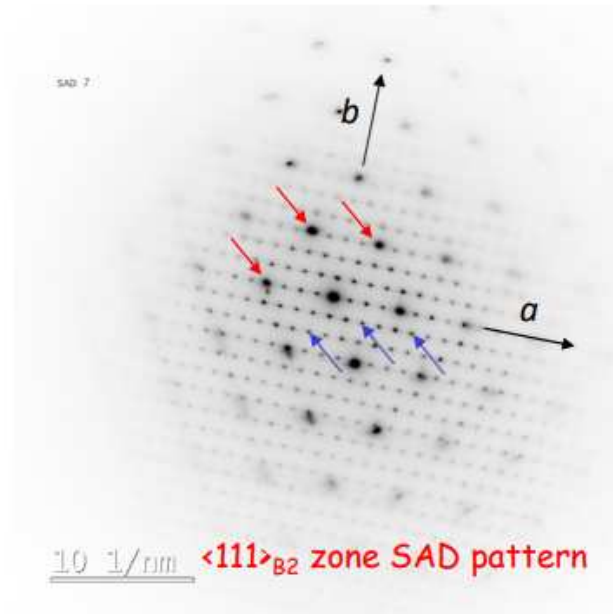


Figure 2.12: Diffraction pattern including spots of the B2 phase (marked with red arrows) and of only the hydride phase (marked with blue arrows); courtesy to A. Dlouhý.

2.4.2 Hydrogen embrittlement

In addition to the theoretical evaluations discussed in this section, practical evaluations on the effects of hydrogen embrittlement in Nitinol have been reported on in Ref. [33] and [34]. The experimental results suggest a significant decrease in fatigue life as well as a decrease in tensile strength (which occurs together with corrosion) due to hydrogen uptake.

Chapter 3

Implementation

3.1 Generation of different starting configurations

Several different starting configurations have been prepared using VESTA. Two experimental evaluations done by Dlouhý and colleagues show that the hydride phase has an orthorhombic unit cell with the lattice parameters $a = 0.8467$ nm, $b = 0.7189$ nm, $c = 0.4737$ nm (first evaluation) or $a = 0.8516$ nm, $b = 0.7246$ nm, $c = 0.5523$ nm (second evaluation), which can be constructed from the B2 structure of NiTi. The orientation relationship between the B2 cell and the orthorhombic supercell is defined by the following relations between lattice directions:

$$\begin{aligned} [1\bar{1}0]_{B2} &\parallel [001]_O \\ [11\bar{2}]_{B2} &\parallel [010]_O \\ [111]_{B2} &\parallel [100]_O \end{aligned}$$

The orthorhombic unit cell is shown in figure 3.1. The lattice parameters used for the construction are $a = 8.50500$ Å, $b = 7.36600$ Å, $c = 5.20800$ Å.

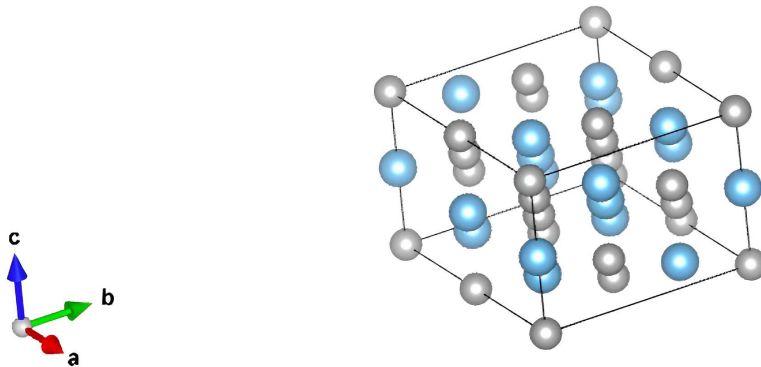


Figure 3.1: Orthorhombic unit cell; nickel atoms displayed in grey; titanium atoms displayed in blue.

The resulting relative positions of nickel and titanium atoms are listed in table 3.3.

Table 3.1: Fractional coordinates of nickel and titanium atoms in the orthorhombic unit cell

nickel positions			titanium positions		
x	y	z	x	y	z
0.00000	0.00000	0.00000	0.00000	0.66667	0.16667
0.25000	0.50000	0.00000	0.25000	0.16667	0.16667
0.50000	0.00000	0.00000	0.50000	0.66667	0.16667
0.75000	0.50000	0.00000	0.75000	0.16667	0.16667
0.00000	0.33333	0.33333	0.00000	0.00000	0.50000
0.25000	0.83333	0.33333	0.25000	0.50000	0.50000
0.50000	0.33333	0.33333	0.50000	0.00000	0.50000
0.75000	0.83333	0.33333	0.75000	0.50000	0.50000
0.25000	0.16667	0.66667	0.00000	0.33333	0.83333
0.00000	0.66667	0.66667	0.50000	0.33333	0.83333
0.75000	0.16667	0.66667	0.25000	0.83333	0.83333
0.50000	0.66667	0.66667	0.75000	0.83333	0.83333

3.1.1 Random hydrogen placement

In order to do a simulation as close as possible to a random starting distribution of hydrogen atoms, random positions in the tetrahedral voids have been chosen. Placing atoms into specific voids ensures that atoms are not accidentally placed too close together and based on previous research, placement in the octahedral voids might result in metastable energy states[31]. The locations of tetrahedral voids in the B2-structure are shown in figure 3.2.

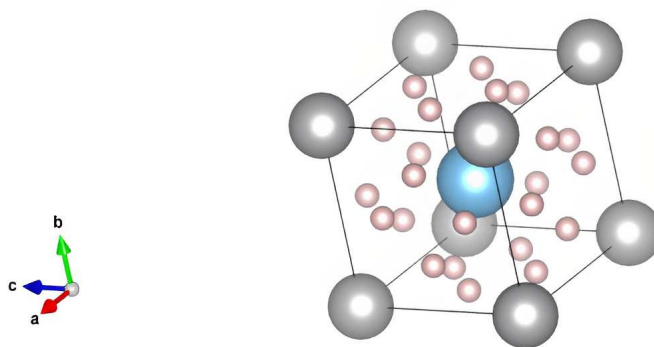


Figure 3.2: Tetrahedral voids in the B2 structure (nickel atoms displayed in grey, titanium atoms displayed in blue and voids filled with light pink hydrogen atoms). Periodic images of atoms on the faces of the cell are included.

The $\text{Ni}_{12}\text{Ti}_{12}$ orthorhombic cell consists of twelve cubic unit cells, each containing twelve tetrahedral voids. This results in a total of 144 possible hydrogen positions. The tetrahedral voids in the cubic B2 cell are located on the (100), (010) and (001) planes. The corresponding hydrogen positions in the orthorhombic cell are shown in figure 3.3.

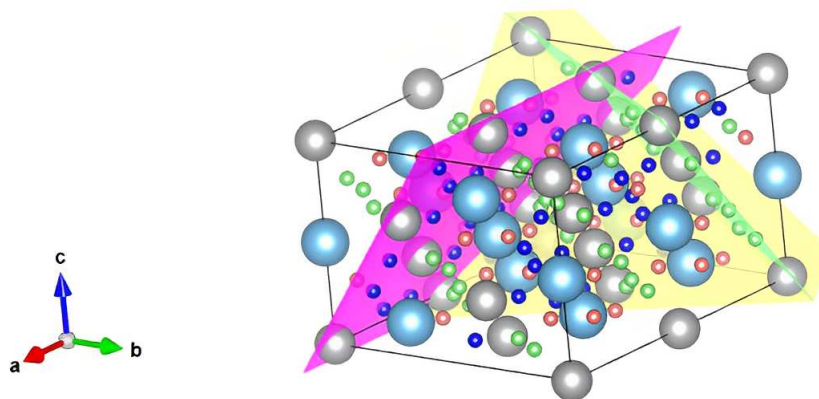


Figure 3.3: Tetrahedral voids in the orthorhombic structure; basal planes of the B2 cell displayed in green, blue and pink; hydrogen colored differently based on the corresponding basal plane.

Out of the possible 144 hydrogen positions, twelve have been chosen using a random number generator. One resulting structure for $\text{Ni}_{12}\text{Ti}_{12}\text{H}_{12}$ with twelve randomly chosen hydrogen atoms is shown in figure 3.4 and the corresponding fractional coordinates are listed in table 3.2.

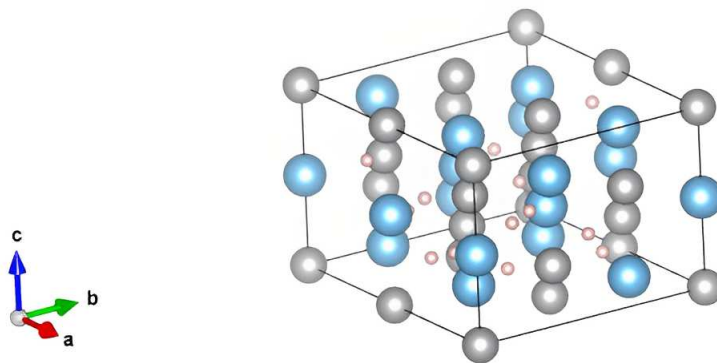


Figure 3.4: Configuration of $\text{Ni}_{12}\text{Ti}_{12}\text{H}_{12}$ with hydrogen atoms placed in random tetrahedral voids (titanium atoms displayed in blue, nickel atoms displayed in grey and hydrogen displayed in light pink).

Table 3.2: Fractional coordinates of twelve randomly chosen tetrahedral voids filled with hydrogen atoms.

x	y	z
0.37500	0.16667	0.41666
0.37500	0.00000	0.75000
0.87500	0.33333	0.58333
0.56250	0.45833	0.08333
0.93750	0.54163	0.41667
0.93750	0.20833	0.58333
0.56250	0.12497	0.25000
0.31250	0.29167	0.41667
0.06250	0.79167	0.41667
0.81250	0.04167	0.41667
0.37500	0.66667	0.41667
0.62500	0.83333	0.08333

3.1.2 Hydrogen placement in nickel-planes

A possible distribution of hydrogen atoms, which fits the experimentally observed diffraction pattern has been proposed by A. Dlouhý and colleagues (see section 2.4.1). It is assumed that hydrogen atoms sit only in positions that are in-plane with nickel atoms (meaning in the basal plane of the original B2 cubic lattice). This resulting hydrogen positions in the cell are shown in figure 3.5 and listed in table 3.3.

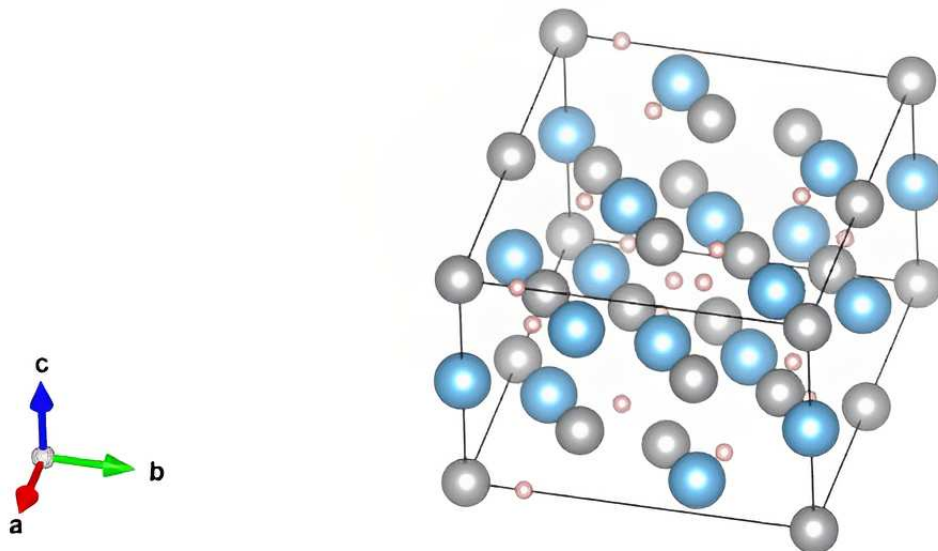


Figure 3.5: Starting configuration with hydrogen placed exclusively into the same lattice planes as nickel atoms (titanium atoms displayed in blue, nickel atoms displayed in grey and and hydrogen displayed in light pink).

Table 3.3: Relative coordinates of hydrogen atoms in Ni-planes.

x	y	z
0.250000000	0.333332986	0.000000000
0.125000000	0.833333015	0.333332986
0.750000000	0.666666985	0.000000000
0.625000000	0.833333015	0.333332986
0.875000000	0.166666999	0.666666985
0.875000000	0.416667014	0.333332986
0.625000000	0.583333015	0.666666985
0.000000000	0.166666999	0.000000000
0.375000000	0.416667014 /0.25	0.333332986
0.375000000	0.166666999	0.666666985
0.125000000	0.750000000	0.666666985
0.500000000	0.833333015	0.000000000

It has to be mentioned that the y -coordinate which is bold in table 3.3 (0.41667) deviates from the position (0.25) which is based on the diffraction pattern. This difference is an error, which has been kept as a variation of the structure, since the relaxation of this alternative structure shows qualitatively different trends in formation energy. (see section 4.1.3) It has thus been considered for further investigation, titled a configuration with “hydrogen mostly in nickel-/titanium-planes” in any plots shown in sections 3.1.2 and 4.1.3). The originally proposed configuration is referred to as a configuration with “hydrogen in nickel-/titanium-planes”.

3.1.3 Hydrogen placement in titanium-planes

In order to create a configuration of hydrogen atoms in titanium planes, the positions of nickel and titanium atoms have been switched. This corresponds to moving the positions of the nickel- and titanium-planes in relation to the hydrogen atoms, which populate the voids. Consequently the hydrogen positions used are the same as for the configuration with hydrogen in nickel-planes described in section 3.1.2.

3.1.4 Hydrogen distributed between Ni- and Ti-planes

In the previous chapters, it was assumed, that hydrogen can populate either nickel- or titanium-planes in a specific pattern. In order to test whether an equal distribution between both planes might lead to energetically more favorable configurations, another starting structure has been created. For this configuration, half of the hydrogen atoms are placed in the nickel planes and the other half are in titanium planes. Since positions in both planes need to be populated, switching the positions of nickel and titanium atoms (and thus moving the planes in relation to the hydrogen atoms) is not an option. In order to place hydrogen atoms into the titanium planes, a vector from the nickel-plane to the titanium plane has been defined as the position of the first titanium atom minus the position of the first nickel atom (which is the origin of the coordinate system). The resulting vector is $[0\frac{2}{3}\frac{1}{8}]$, expressed in relative coordinates of the orthorhombic cell and is shown in figure 3.6.

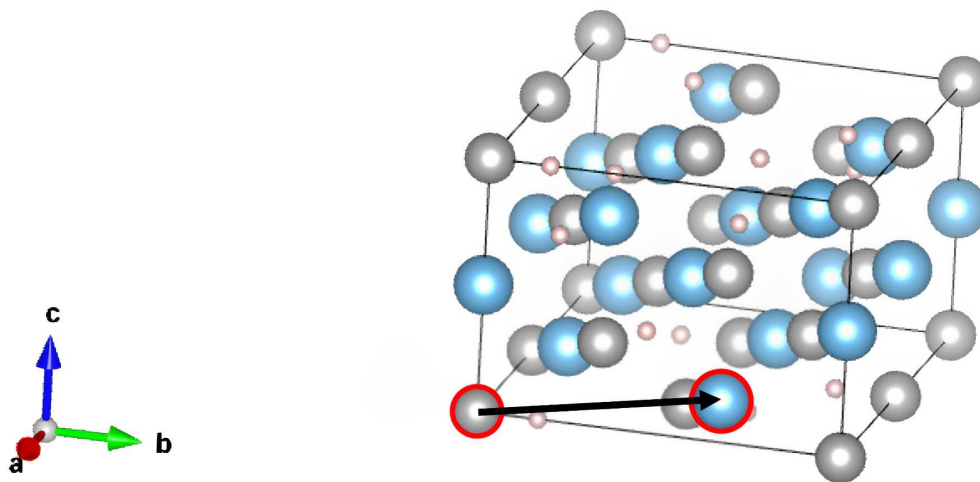


Figure 3.6: Translational vector between positions in nickel- and titanium planes (nickel atoms displayed in grey, titanium atoms displayed in blue).

Out of the 24 possible positions (12 in titanium planes; 12 in nickel planes), 12 (6 in titanium-planes; 6 in nickel-planes) have been chosen for the final structure as listed in table 3.4.

Table 3.4: Relative coordinates of hydrogen atoms in Ni or Ti-planes.

x	y	z	plane
0.25000000	0.333332986	0.00000000	Ni
0.25000000	0.00000000	0.166666999	Ti
0.12500000	0.50000000	0.50000000	Ti
0.37500000	0.833334029	0.833334029	Ti
0.62500000	0.833333015	0.333332986	Ni
0.87500000	0.833334029	0.833334029	Ti
0.50000000	0.833333015	0.00000000	Ni
0.37500000	0.166666999	0.666666985	Ni
0.12500000	0.833333015	0.333332986	Ni
0.62500000	0.583333015	0.666666985	Ni
0.87500000	0.083333969	0.50000000	Ti
0.75000000	0.00000000	0.166666999	Ti

3.1.5 Hydrogen placement in the first octant of the supercell

To assess, whether clustering of hydrogen atoms within the unit cell is more energetically favorable than an even distribution, a starting configuration with very

closely packed hydrogen positions has been created. In the first step of creating this configuration, out of all the tetrahedral voids, only the ones in the first octant of the cell have been considered. From those positions, the ones which are the furthest away from the origin have been removed one by one until only 12 positions remained. The resulting structure is shown in figure 3.7 and the positions are listed in table 3.5.

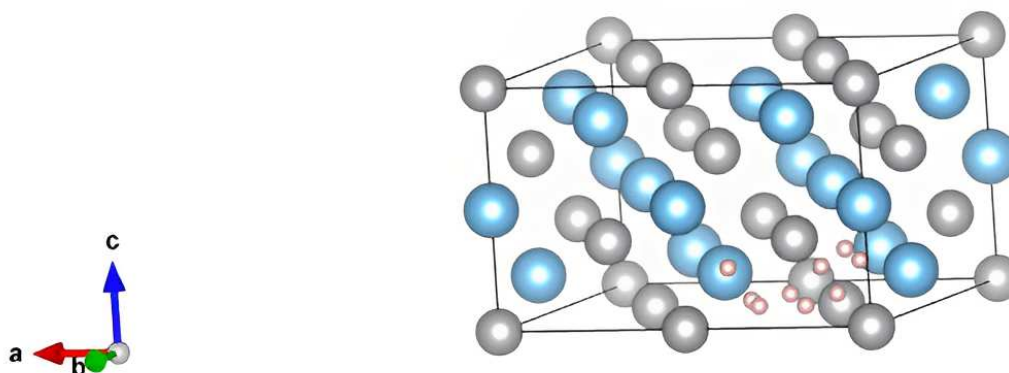


Figure 3.7: Unit cell with hydrogen only in the first octant.

Table 3.5: Relative coordinates of hydrogen atoms for a configuration with clustered hydrogen atoms.

x	y	z
0.083332002	0.041668002	0.312500000
0.083330996	0.166666999	0.374998987
0.083299004	0.291700006	0.187500000
0.083330996	0.291667998	0.312498987
0.083333001	0.041666999	0.187500000
0.249999002	0.375000000	0.187499002
0.250007987	0.000000000	0.125000000
0.249964997	0.375034004	0.312500000
0.249997005	0.000000000	0.374998987
0.416664988	0.333332986	0.125000000
0.416666001	0.208333999	0.062500000
0.250000000	0.125000000	0.062500000

3.2 Evaluation of the energetic stability

To assess the energetic stability of the different starting configurations, the formation energy and the mixing enthalpy per atom have been calculated for the relaxed structures using the different starting configurations described in section 3.1 and different numbers of hydrogen atoms (0, 2, 4, 6, 8, 10 and 12 as well as 14 and 16, which is higher than content proposed by Dlouhý and colleagues). In the following, the methodology for calculating the formation energy and the mixing enthalpy is explained.

3.2.1 Formation energy

The formation energy of a structure is the difference between its ground state energy and the sum of the formation energies of all its individual components in their most stable state [35]. In the case of $\text{Ni}_{12}\text{Ti}_{12}\text{H}_x$, the individual components in their most stable state are metallic fcc nickel, metallic hcp titanium and one half of molecular H_2 for each hydrogen atom in the cell. The calculated individual chemical potentials are listed in table 3.6. The parameters used to calculate the chemical potentials using VASP can be found in the appendix.

Table 3.6: Chemical potentials of elements in $\text{Ni}_{12}\text{Ti}_{12}\text{H}_x$ in their most stable state.

Phase	Chemical potential μ [eV]
fcc Ni	-5.4606
hcp Ti	-7.8332
H_2	-3.3811

To calculate the formation energy per atom for a given structure, $\varepsilon_F^{\text{Ni}_{12}\text{Ti}_{12}\text{H}_x}$, equation 3.1 has been applied:

$$\varepsilon_F^{\text{Ni}_{12}\text{Ti}_{12}\text{H}_x} = \frac{E^{\text{Ni}_{12}\text{Ti}_{12}\text{H}_x} - \mu^{\text{Ni}_{fcc}} \cdot 12 - \mu^{\text{Ti}_{hcp}} \cdot 12 - \mu^{\text{H}_2} \cdot \frac{x}{2}}{24 + x} \quad (3.1)$$

$E^{\text{Ni}_{12}\text{Ti}_{12}\text{H}_x}$ is the total energy of the relaxed cell, which is compared to the individual elements in their most stable phases represented by the chemical potentials $\mu^{\text{Ti}_{hcp}}$, $\mu^{\text{Ni}_{fcc}}$ and $\mu^{\text{H}_2} \cdot \frac{x}{2}$, which are each multiplied with the respective number of atoms in the cell to be examined. The difference between the total energy and the sum of the chemical potential then gives the energy difference between the relaxed

supercell and the same elements in their most stable configurations. To get the formation energy of the whole cell, this energy is divided by the total number of atoms in the supercell.

3.2.2 Mixing enthalpy

A different approach for evaluating the energetic stability of a structure is by calculating the mixing enthalpy using equation 3.2. The distinguishing factor from the formation energy is that the ground state energy of the hydride phase is not compared to the chemical potentials of the individual components, but to the total energy of a pure $\text{Ni}_{12}\text{Ti}_{12}$ matrix, and molecular hydrogen outside the metal [35]. A negative mixing energy indicates that hydrogen atoms tend to diffuse into the matrix as opposed to staying in their gaseous form. The formula used to calculate the mixing enthalpy is shown in the following. $E^{\text{Ni}_{12}\text{Ti}_{12}}$ is the energy resulting from fully relaxing configurations of $\text{Ni}_{12}\text{Ti}_{12}\text{H}_x$ for $x = 0$.

$$\epsilon_{mix}^{\text{Ni}_{12}\text{Ti}_{12}\text{H}_x} = \frac{E^{\text{Ni}_{12}\text{Ti}_{12}\text{H}_x} - E^{\text{Ni}_{12}\text{Ti}_{12}} - \mu^{\text{H}_2} \cdot \frac{x}{2}}{24 + x} \quad (3.2)$$

3.3 Evaluation of the energetic stability of geometrically confined cells

In STEM-images of the cell, as shown in figure 3.8, the precipitated hydride phase is found completely embedded within the B2 matrix in a thin needle-like shape. This suggests, that the unit cell of the hydride phase is somewhat geometrically confined. The cell shape and size can be fixed during relaxation when using the parameter $\text{ISIF} = 2$ in the INCAR file. All configurations have been relaxed using this setting in order to compare them to the fully relaxed structures, which correspond to the standalone hydride.

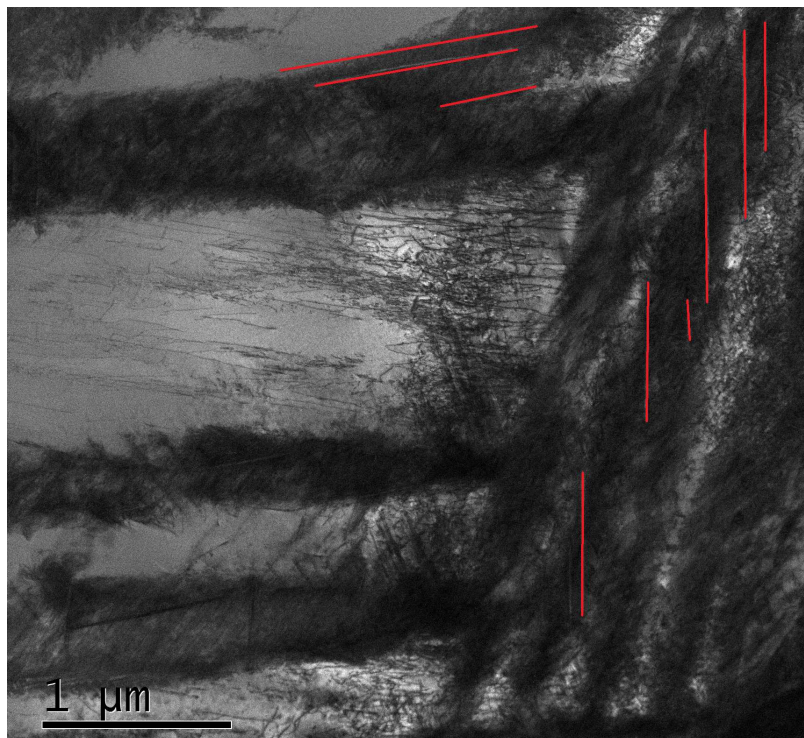


Figure 3.8: STEM-image of hydride phase precipitates in B2-NiTi matrix (marked with red lines); courtesy to A. Dlouhý.

3.4 Evaluation of the equilibrium lattice parameters of partially confined cells

For another approach to approximate the cell shape, it is assumed that the hydride phase can locally change the lattice parameters by stretching the lattice, but does not change the cell angles. This has been simulated using two different approaches — either by keeping the ratio of cell parameters the same and scaling up the volume or by changing the cell parameters individually.

This process cannot be automated in VASP, so the lattice parameters have been fitted manually. Decent accuracy could be reached quickly for a fixed ratio between lattice parameters. For the individually fitted lattice parameters, the first rough estimate has been supplemented with a more precise one using the Gadget code [36]. With the Gadget code, different constraints can be applied to a unit cell during relaxation steps, in this case specifically, the cell angles have been fixed. Using a starting configuration that has already been manually fitted ensures that the structure does not relax into a metastable state. Furthermore, it reduces the computational time.

3.5 Evaluation of hydrogen distribution

In order to quantify how hydrogen atoms are distributed within the unit cell and to find a correlation with the energy, a few python scripts have been written. A link to the code can be found in the appendix.

The scripts are used to calculate:

- (a) ...the average distance between each hydrogen atom and its nearest nickel neighbor
- (b) ...the average distance between each hydrogen atom and its nearest titanium neighbor
- (c) ...the average distance between each hydrogen atom and its closest other hydrogen atom

The different methods of evaluation are schematically depicted in figure 3.9.

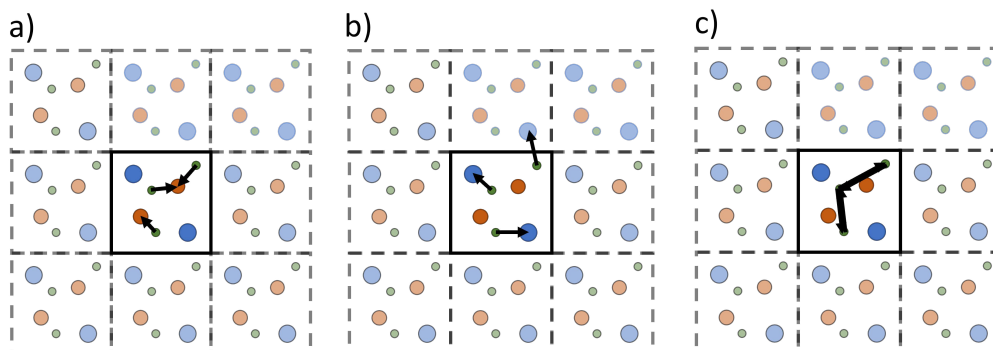


Figure 3.9: Different strategies for quantifying the hydrogen distribution. Green, red and blue atoms schematically represent hydrogen, nickel and titanium atoms respectively.

3.6 Evaluation of mechanical stability

In addition to the evaluation of the energetic stability, the mechanical stability of the relaxed cells has been assessed by calculating the elastic constants. Negative elastic constants indicate mechanical instability, meaning that the respective cell structure cannot exist without being stabilized by a matrix.

3.6.1 The stress-strain method

The method used for evaluating the elastic constants is the stress-strain method [37]. A fixed strain is applied to the unit cell. It is then relaxed using the ISIF = 2 setting (fixed cell parameters). Hooke's law states that the relation between the stresses and strains in the Voigt's notation is defined by equation 3.3.

$$\begin{pmatrix} \sigma_x \\ \sigma_y \\ \sigma_z \\ \sigma_{xz} \\ \sigma_{yz} \\ \sigma_{xy} \end{pmatrix} = \begin{pmatrix} C_{11} & C_{12} & C_{13} & C_{14} & C_{15} & C_{16} \\ C_{21} & C_{22} & C_{23} & C_{24} & C_{25} & C_{26} \\ C_{31} & C_{32} & C_{33} & C_{34} & C_{35} & C_{36} \\ C_{41} & C_{42} & C_{43} & C_{44} & C_{45} & C_{46} \\ C_{51} & C_{52} & C_{53} & C_{54} & C_{55} & C_{56} \\ C_{61} & C_{62} & C_{63} & C_{64} & C_{65} & C_{66} \end{pmatrix} \begin{pmatrix} \varepsilon_x \\ \varepsilon_y \\ \varepsilon_z \\ \varepsilon_{xz} \\ \varepsilon_{yz} \\ \varepsilon_{xy} \end{pmatrix} \quad (3.3)$$

Using the residual stresses resulting from the relaxation and the initially applied strains, the elastic constants can be calculated. Furthermore, for the orthorhombic cell shape, the matrix representing the elastic tensor can be simplified as:

$$\begin{pmatrix} C_{11} & C_{12} & C_{13} & 0 & 0 & 0 \\ C_{21} & C_{22} & C_{23} & 0 & 0 & 0 \\ C_{31} & C_{32} & C_{33} & 0 & 0 & 0 \\ 0 & 0 & 0 & C_{44} & 0 & 0 \\ 0 & 0 & 0 & 0 & C_{55} & 0 \\ 0 & 0 & 0 & 0 & 0 & C_{66} \end{pmatrix}$$

The calculation of the elastic constants for using VASP proceeds via applying six different linearly independent strains of equal magnitude to the cell in both tensile and compressive direction (resulting in twelve strain vectors used to independently calculate the elastic constants). The strain magnitude *delta* has been chosen in order to be distinctly in the linear elastic regime, but not so small that numerical inaccuracies significantly affect the results. The code used to define the different stresses is shown in the following:

```
01 # define strain magnitude
02 delta = 0.003
03 # define strain vector
04 strains = np.array([
05     np.array([ 1, -2,  3, -4,  5, -6])/6.0,
06     np.array([ 2,  1, -5, -6,  4,  3])/6.0,
07     np.array([ 3,  4, -1,  5,  5, -2])/6.0,
08     np.array([ 4, -3,  6,  1, -2,  5])/6.0,
09     np.array([ 5,  6,  2, -3, -1, -4])/6.0,
10     np.array([ 6, -5, -4,  2, -3,  1])/6.0
11 ])
12
13 strains = [sign*delta*s for sign in (-1, 1) for s in strains]
```

Visually displaying the elastic tensor is made possible using the “ELATE: Elastic Tensor Analysis” online tool [38]. Furthermore, the eigenvalues of the elastic matrix are automatically calculated.

Chapter 4

Determination of phase stability

4.1 Energy per atom for fully relaxed cells

The following sections describe the trends in the formation energy and mixing enthalpy for cells that were fully relaxed from the different starting configurations described in section 3.1. To evaluate the influence that different amounts of hydrogen have on the phase stability, hydrogen atoms are added to the unit cell in increments of two atoms, up to a configuration of $\text{Ni}_{12}\text{Ti}_{12}\text{H}_{16}$.

4.1.1 Random hydrogen placement

Figure 4.1 shows the formation energy and the mixing enthalpy against the number of hydrogen atoms in the cell for a starting configuration with hydrogen randomly distributed throughout the tetrahedral voids (as described in section 3.1.1).

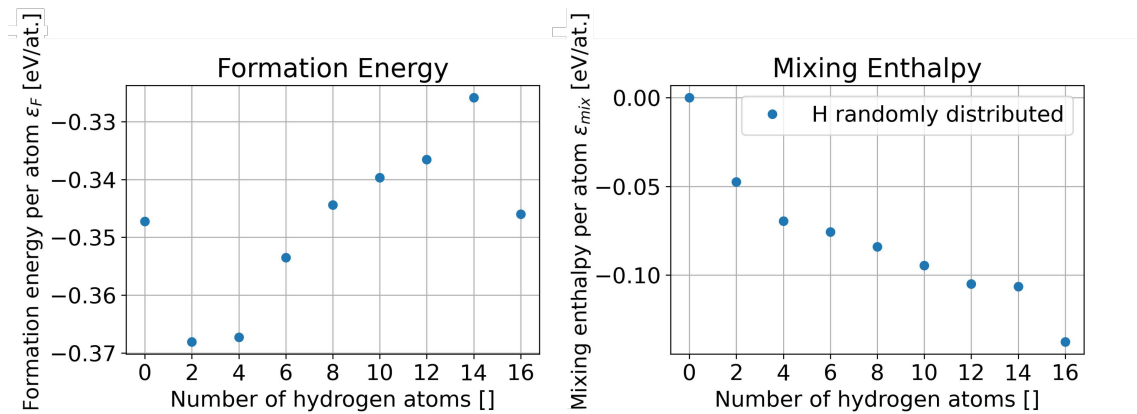


Figure 4.1: (Left) formation energy/(right) mixing enthalpy against number of randomly distributed hydrogen atoms in the cell.

There is a notable trend in the formation energy and even more in the mixing enthalpy, where some hydrogen in the cell ($\text{Ni}_{12}\text{Ti}_{12}\text{H}_2$ and $\text{Ni}_{12}\text{Ti}_{12}\text{H}_4$) leads to a significant drop in energy from the structure without hydrogen. This signifies a drive for hydrogen atoms to exist as solutes in the structure, as opposed to staying in their gaseous form. Another interesting fact about this configuration is that there is a drop in energy for $\text{Ni}_{12}\text{Ti}_{12}\text{H}_{16}$. The origin of this behavior will be explored in section 4.3. The energies for the configurations with randomly placed hydrogen will be displayed in the subsequent plots (as a reference).

4.1.2 Hydrogen placement in nickel planes

In the following diagram (figure 4.2), the formation energy and mixing enthalpy against the number of hydrogen atoms in the cell are displayed for the two starting configurations described in section 3.1.2 (“H mostly in Ni planes” and “H in Ni planes”).

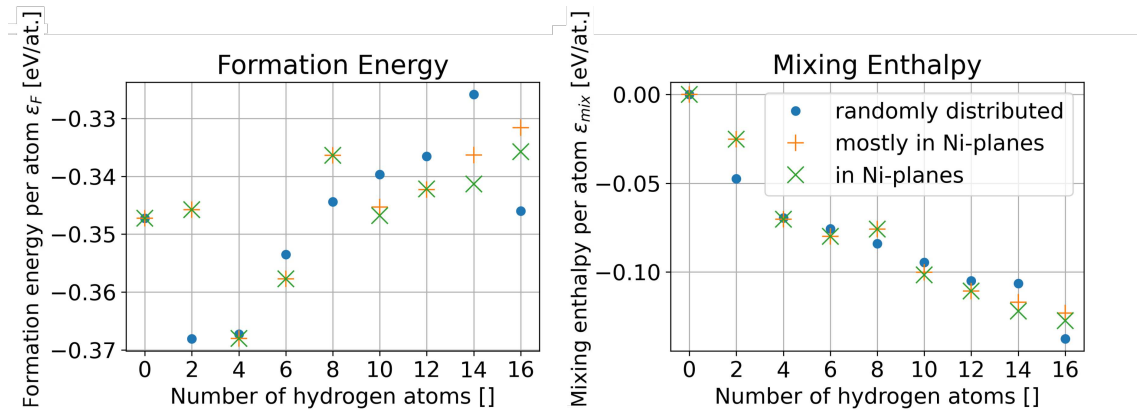


Figure 4.2: (Left) formation energy/(right) mixing enthalpy against number of hydrogen atoms in or mostly in Ni planes.

When looking at the trends in formation energy, deviations from the behavior exhibited by the random starting configuration can be observed. Most notably, the structure of $\text{Ni}_{12}\text{Ti}_{12}\text{H}_2$ is significantly more energetically unfavorable — even more so than the structure without hydrogen. The possible reasons will be explored in section 4.3. Furthermore, there is no energy minimum at higher amounts of hydrogen. Since the expected content of hydrogen is approximately 33 at.% (see [32]), this starting configuration does not seem to relax into the expected structure of the hydride.

4.1.3 Hydrogen placement in titanium planes

In figure 4.3 the relaxed structures resulting from the starting configurations with hydrogen “in titanium planes” or “mostly in titanium planes” as described in section 4.1.3 are plotted.

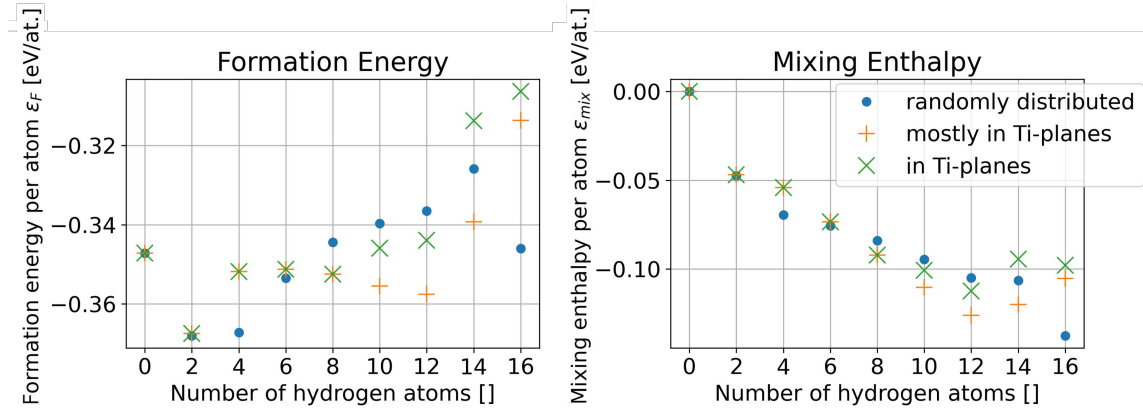


Figure 4.3: (Left) formation energy/(right) mixing enthalpy against number of hydrogen atoms in or mostly in Ti planes.

For a low hydrogen content, the behavior is qualitatively the same as for the random starting configuration.

4.1.4 Hydrogen placement in both nickel and titanium planes

The structure with hydrogen atoms distributed between both nickel and titanium planes described in section 3.1.4 has been relaxed with different hydrogen contents. The results are shown in figure 4.4.

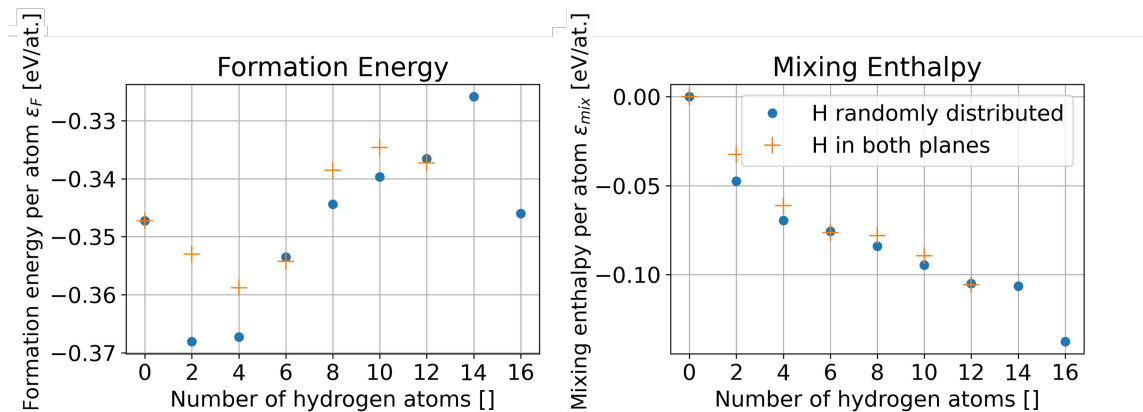


Figure 4.4: (Left) formation energy/(right) mixing enthalpy against number of hydrogen atoms distributed between Ni and Ti planes.

It has to be noted that relaxations for 14 and 16 hydrogen atoms have been performed, however both yielded only unreasonable structures (the structures completely disassembled during relaxation), suggesting that too many atoms were placed too close together for the starting configurations.

4.1.5 Clustered hydrogen configuration

In figure 4.5, the resulting formation energies and mixing enthalpies from the relaxation of the unit cell with an artificial hydrogen cluster are shown.

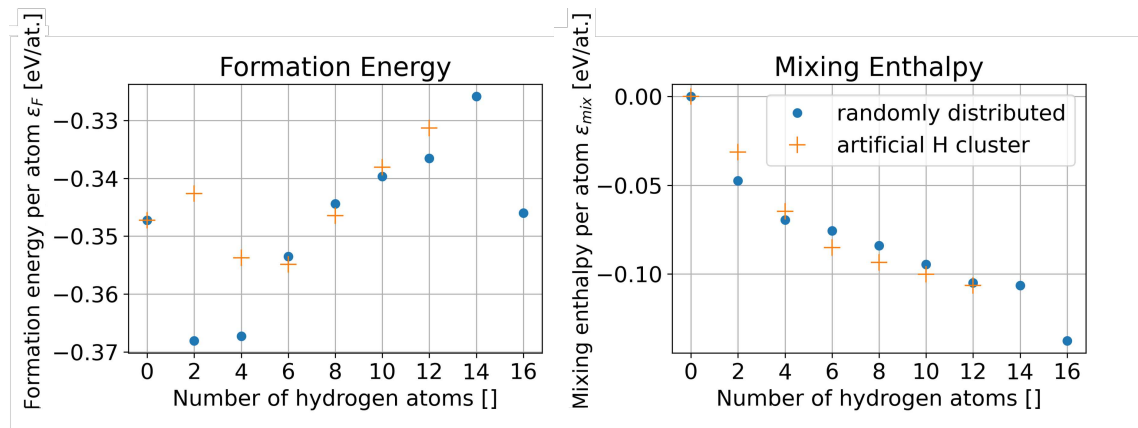


Figure 4.5: (Left) formation energy/(right) mixing enthalpy against number of clustered hydrogen atoms in the cell.

When looking at the trends in formation energy, there is an unexpectedly high value at two hydrogen atoms similar to what is observed for the configuration with hydrogen in nickel planes (see section 4.1.2). The origin of this phenomenon is further explored in section 4.3.

It has to be noted that calculations for 14 and 16 hydrogen atoms have not been performed due to the fact that this would have filled up a large portion of the cell, defeating the purpose of creating an isolated “cluster” in the unit cell. Whether the cluster is still present in the relaxed structure will also be assessed in section 4.3.

4.2 Energy per atom for confined cells

Due to the fact that the hydride phase exhibits a macroscopically needle-like shape embedded into the B2 matrix, as shown in figure 3.8, a second set of calculations, where only the atomic positions and not the lattice parameters are relaxed, was performed. In the following diagram, the results from the relaxation of just the atomic positions are compared to each other.

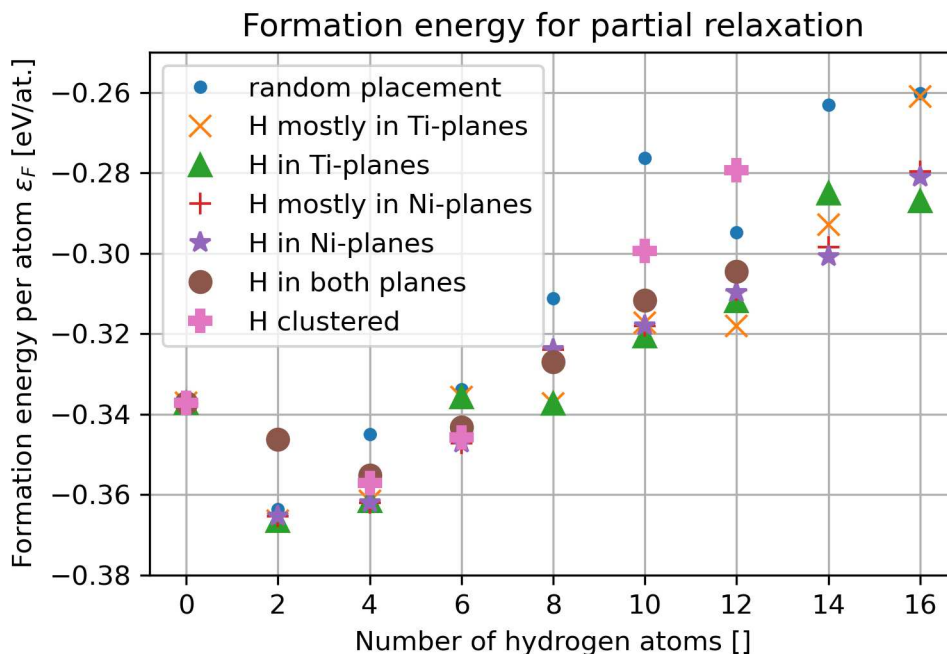


Figure 4.6: Formation energy for different starting configurations after partial relaxation.

It has to be mentioned that specifically some configurations with more than 12 hydrogen atoms are energetically unstable. The energy per atom for the different configurations of $\text{Ni}_{12}\text{Ti}_{12}\text{H}_{12}$ for full and partial relaxation, as well as their equilibrium monoclinic angles are listed in table 4.1. The comparison for slightly different amounts of hydrogen would have yielded similar results, but this configuration has been chosen, because it is the stoichiometry initially proposed by Dlouhý and colleagues.

Table 4.1: Energy per atom and monoclinic angles for different structures of $\text{Ni}_{12}\text{Ti}_{12}\text{H}_{12}$ after relaxation.

Configuration	E/atom [eV/at.] (full relaxation)	E/atom [eV/at.] (partial relaxation)	smallest angle [deg]
random	-5.895	-5.853	88.828
in Ni planes	-5.901	-5.868	87.942
mostly in Ni planes	-5.901	-5.867	88.384
in Ti planes	-5.902	-5.870	87.324
mostly in Ti planes	-5.916	-5.876	86.124
in both planes	-5.896	-5.863	89.021
clustered	-5.890	-5.838	85.907

The structure, which includes a cluster, although it has a very small monoclinic angle, still has the highest energy when fully relaxed. This suggests, that clustering of hydrogen atoms is unfavorable.

Looking at the other structures, there is a distinct pattern that a more monoclinic shape of the fully relaxed cell correlates with a lower formation energy. The structure, which has the most monoclinic shape when fully relaxed (hydrogen mostly in Ti planes) has the largest difference between the formation energies of full and partial relaxation. It can be considered the most energetically favorable, even in its partially relaxed state.

4.2.1 Relationship between energy per atom and cell shape

In section 4.2, it has been found that the structure, which exhibits the lowest monoclinic angle has the lowest energy per atom (if the energetically unfavorable clustered configuration is excluded). Furthermore, it has been shown that the difference between energies of a set of configurations is diminished, when the constraints of a fixed cell shape and size are applied. This observation agrees with the expectation that a monoclinic phase should be more energetically favorable, because DFT calculations are performed at 0K. At this temperature, for pure NiTi, the monoclinic B19' phase is the stable configuration. The experiments performed by Dlouhý and colleagues, who found the hydride phase in a B2 matrix, were performed at temperatures where the B2 matrix is the stable phase. The results of the relaxation with constraints might thus be more practically relevant. In chapter 5, a further optimization of these constraints will be performed to more realistically approximate the confinement of the hydride phase in a B2 matrix.

4.3 Correlation of energy with hydrogen distribution

The different methods for evaluating the hydrogen distribution mentioned in section 3.5 have been applied to a few different configurations in order to find patterns in the hydrogen distribution. Furthermore, cells have been visually compared. This section will focus specifically on a few configurations, which have unexpectedly high or low formation energy. These include the most energetically favorable configuration of “H mostly in Ti planes” with 12 H-atoms in comparison to “H mostly in Ni planes”, as an example for a less energetically favorable configuration.

A relaxed structure from the starting configuration with hydrogen in the first octant of the cell is also examined to find out, whether clusters persist after relaxation. Lastly, the configuration of $\text{Ni}_{12}\text{Ti}_{12}\text{H}_2$ with hydrogen in Ni planes (see figure 4.2) and in a cluster (see figure 4.5) will be discussed due to their extremely high formation energy (which is higher than for pure NiTi).

Lastly, the very low energy configuration of $\text{Ni}_{12}\text{Ti}_{12}\text{H}_{16}$ from a random starting configuration will be touched on.

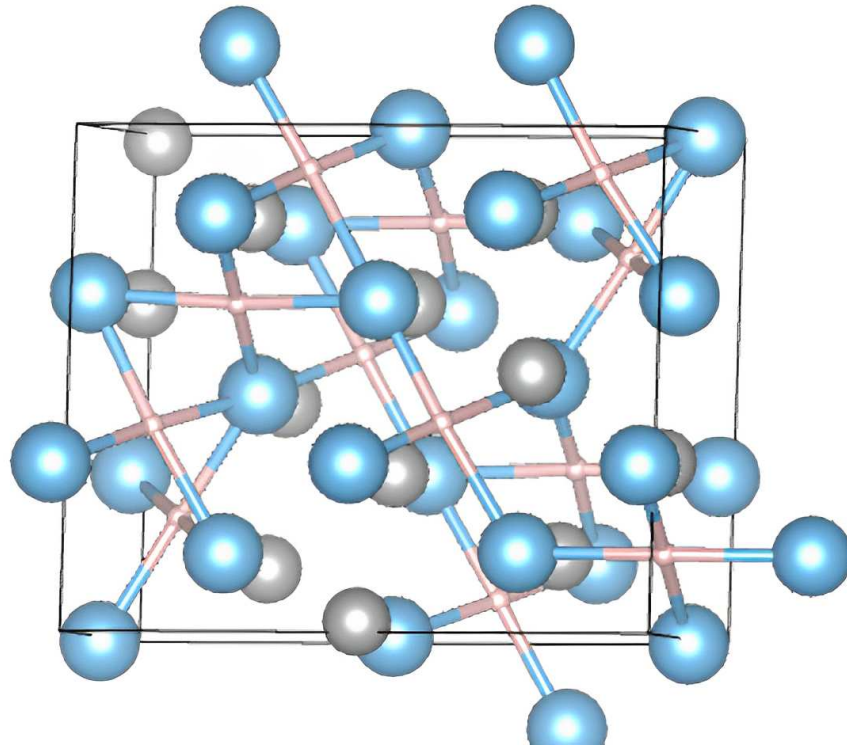


Figure 4.7: Fully relaxed $\text{Ni}_{12}\text{Ti}_{12}\text{H}_{12}$ with H mostly in Ni planes.

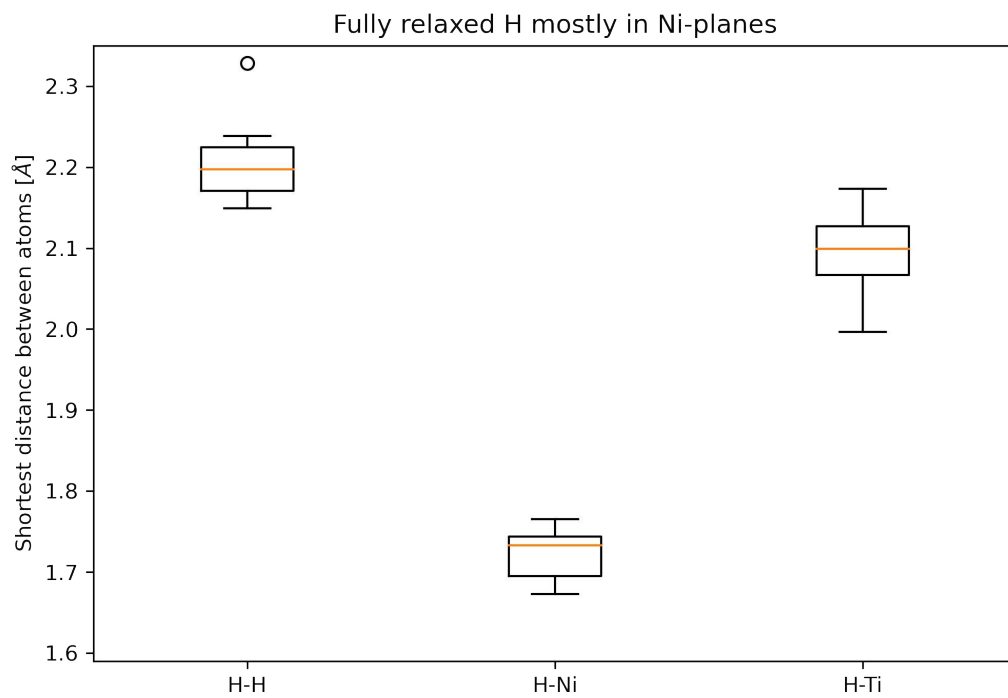


Figure 4.8: Minimal distances between different atom types for fully relaxed $\text{Ni}_{12}\text{Ti}_{12}\text{H}_{12}$ with H mostly in Ni planes.

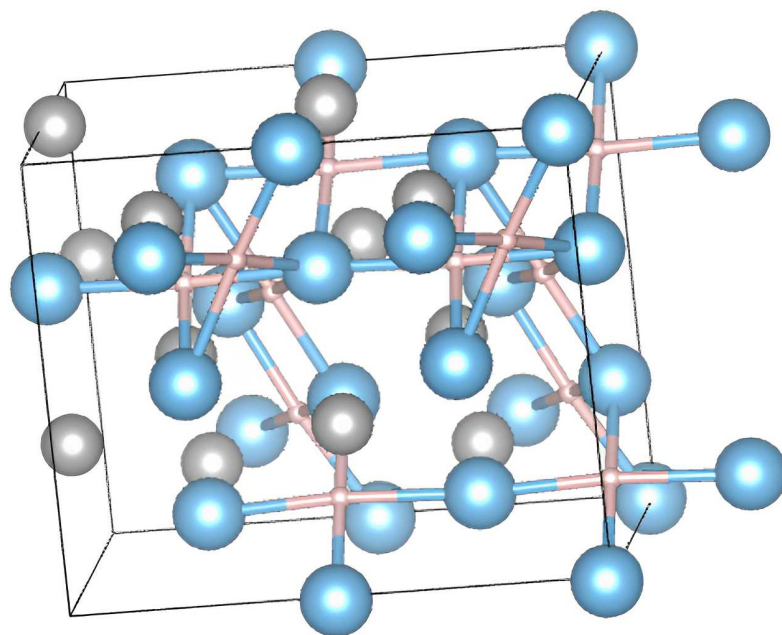


Figure 4.9: Fully relaxed $\text{Ni}_{12}\text{Ti}_{12}\text{H}_{12}$ with H mostly in Ti planes.

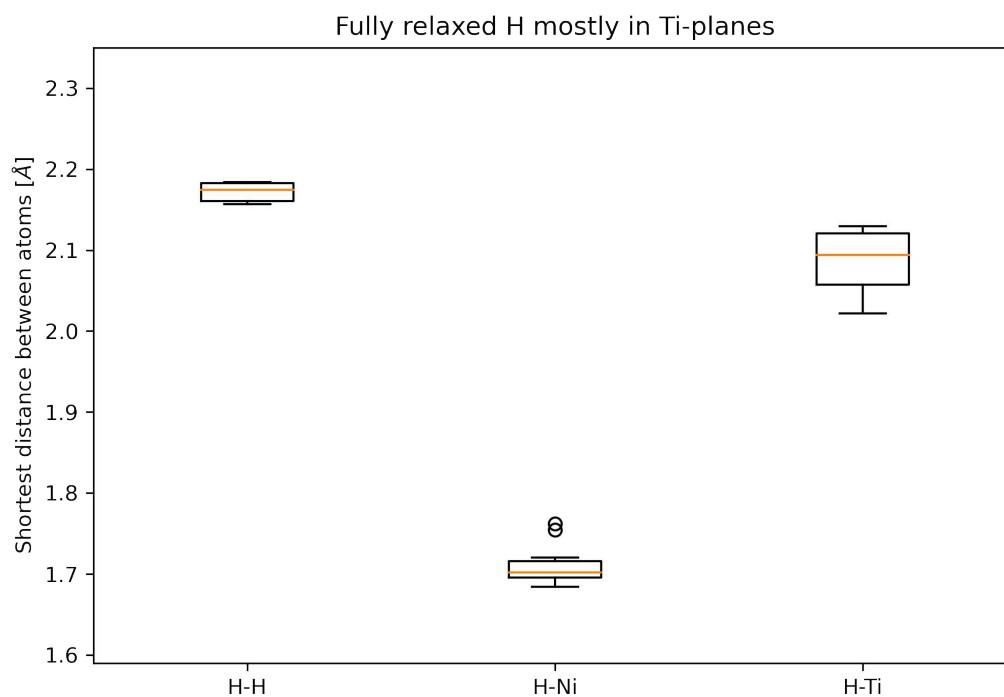


Figure 4.10: Minimal distances between different atom types for fully relaxed $\text{Ni}_{12}\text{Ti}_{12}\text{H}_{12}$ with H mostly in Ti planes.

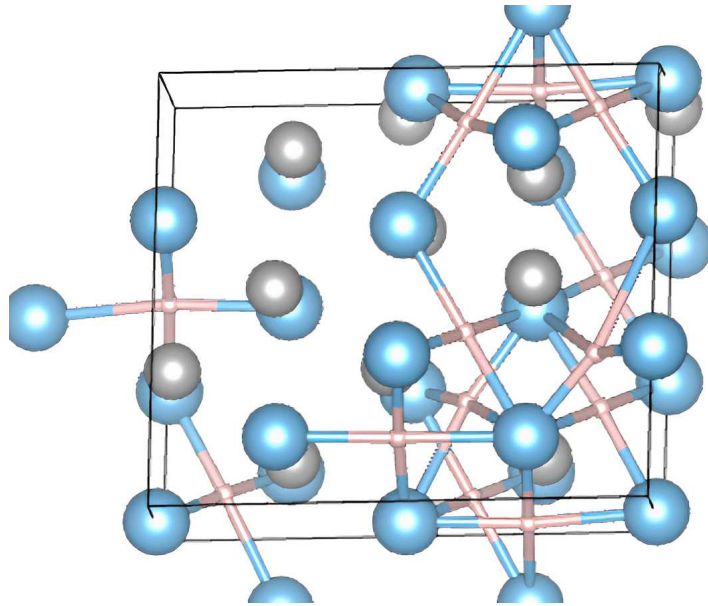


Figure 4.11: Fully relaxed $\text{Ni}_{12}\text{Ti}_{12}\text{H}_{12}$ with a clustered starting configuration.

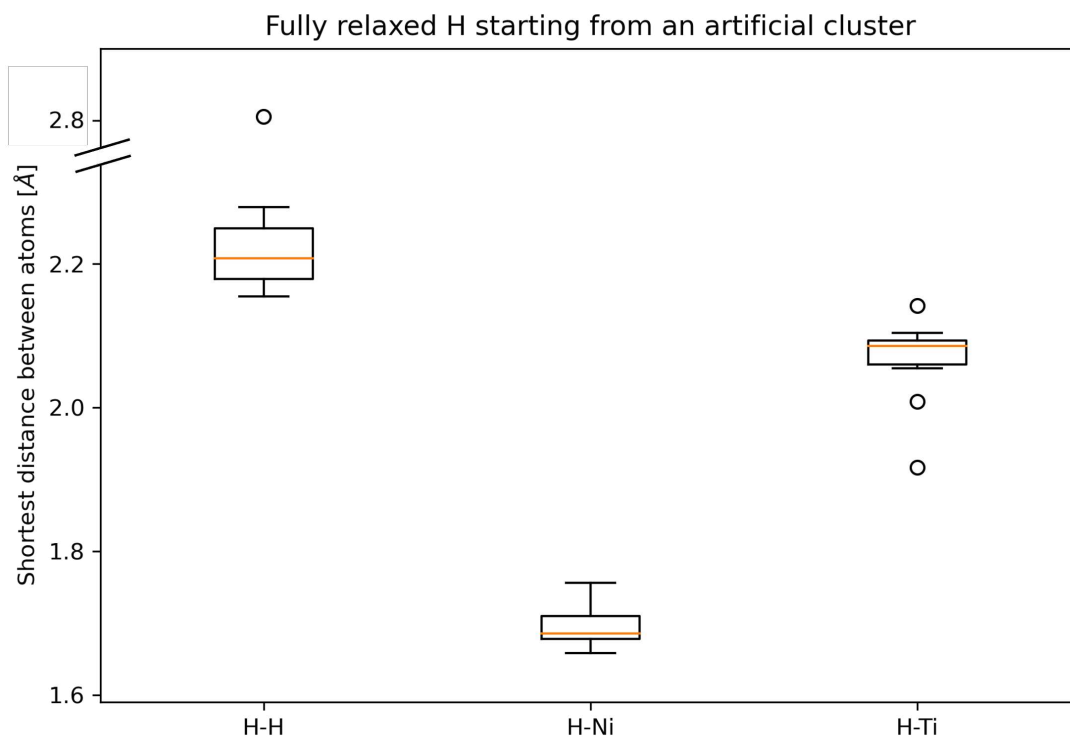


Figure 4.12: Minimal distances between different atom types for fully relaxed $\text{Ni}_{12}\text{Ti}_{12}\text{H}_{12}$ with a clustered starting configuration.

Looking at the different hydrogen positions in the cell it becomes clear that the most favorable position for hydrogen is slightly off-center in the octahedral voids in Ti planes as it was also found by Holec et al. [31]. There is not a single hydrogen in a different interstitial position.

The most interesting difference between the most energetically favorable distribution in figure 4.9 and another configuration such as the one in figure 4.7 is that the energetically stable configuration exhibits additional translational symmetry of hydrogen distribution within the cell. The same configuration of six hydrogen positions is occupied twice twice in the cell.

When looking at the clustered starting configuration, there seems to be a tendency for hydrogen atoms to spread throughout the cell.

When comparing the distributions of hydrogen atoms, there is a small difference to be found between the most energetically favorable configuration in figure 4.10 and a less favorable configuration in figure 4.8. Namely, the spread for all different minimum distances is smaller and the average distance between hydrogen atoms is also slightly smaller with a distinctly low spread of the values. However, this may not be the direct cause for the lower energy as in the most energetically favorable structure, there is a periodicity in the hydrogen positions, which also leads to a lower spread of the values.

What is interesting about the clustered configuration in figure 4.12 is that the distances of the relaxed structure are very similar to those of the other configurations apart from a few outliers. Specifically, the mean values are almost identical to those of the other configurations. This would suggest, that the optimal equilibrium hydrogen distance is simply not small enough to facilitate clustering.

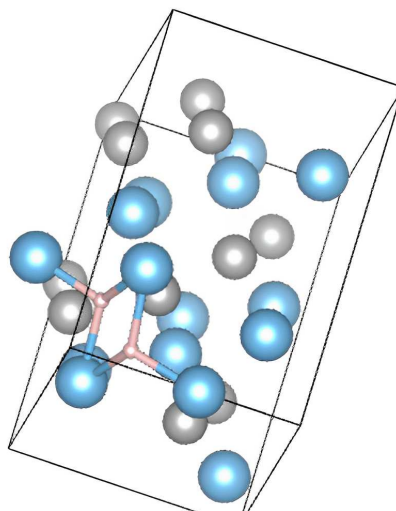


Figure 4.13: Fully relaxed $\text{Ni}_{12}\text{Ti}_{12}\text{H}_2$ with a clustered starting configuration with bonds to the closest Ti-atoms displayed.

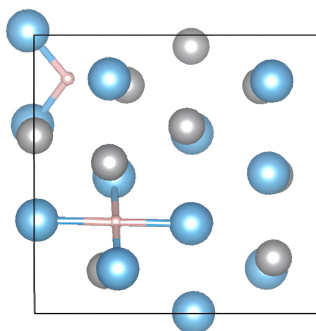


Figure 4.14: Fully relaxed $\text{Ni}_{12}\text{Ti}_{12}\text{H}_2$ with a starting configuration in nickel planes with bonds to the closest Ti-atoms displayed.

The two configurations of $\text{Ni}_{12}\text{Ti}_{12}\text{H}_2$ with very high energy are shown in figures 4.13 and 4.14. What they have in common is that at least one of their hydrogen atoms is located in a tetrahedral void. The fact that their energy is significantly higher than for other configurations further supports the hypothesis that positions in octahedral voids are more favorable.

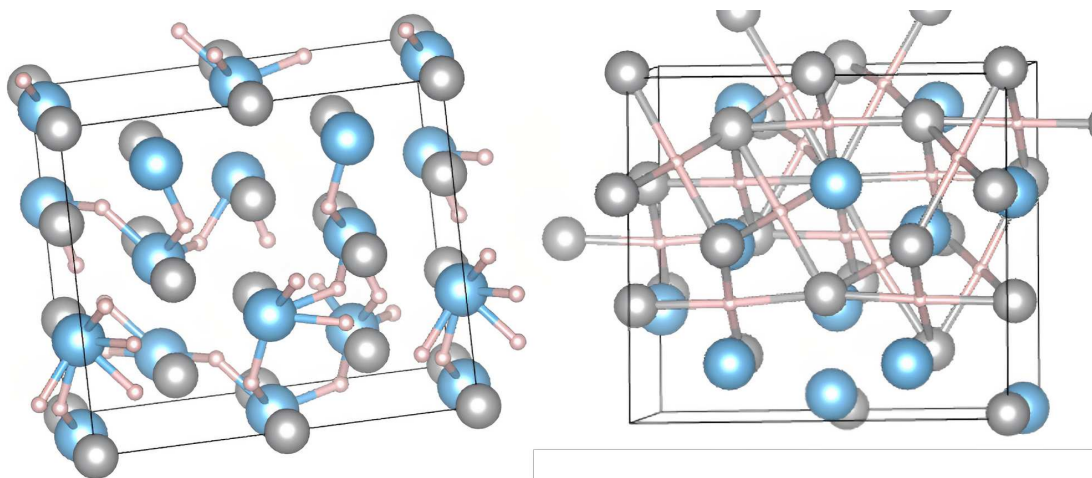


Figure 4.15: Random starting configuration for $\text{Ni}_{12}\text{Ti}_{12}\text{H}_{16}$ (left) and fully relaxed $\text{Ni}_{12}\text{Ti}_{12}\text{H}_{16}$ with bonds to the closest Ni-atoms displayed (right).

The structure of the very low energy configuration of $\text{Ni}_{12}\text{Ti}_{12}\text{H}_{16}$ found in figure 4.1 is shown in figure 4.15. Remarkably, all hydrogen atoms relaxed into octahedral voids in Ni planes instead of Ti planes in this case, which is not seen in any other configuration. Due to the fact that no similar configuration is seen in any other structure and at this large amount of hydrogen, some other structures did not relax at all, it will not be considered for further evaluation, but it could be an interesting topic for future research.

4.4 Elastic constants of relaxed cells

The elastic constants of the most energetically stable configuration of the $\text{Ni}_{12}\text{Ti}_{12}\text{H}_{12}$ hydride phase (mostly in Ti planes) and a less stable configuration (mostly in Ni planes; see section 4.1) have been calculated and compared to those of the B2 matrix in order to assess the mechanical stability and get an estimate for the elastic properties and anisotropy of the cell (see section 3.6.1). The elastic constants have been calculated for the completely relaxed cell as well as for the confined cell. The tensors of elastic constants for the different phases can be found in the appendix. The results for the shear moduli, Young's moduli and Poisson's ratios are listed in tables 4.2, 4.3, 4.4 and 4.5. It has to be noted that the fully relaxed structure with H mostly in Ni planes is not mechanically stable. In table 4.6, the average properties (calculated using the Voigt's scheme) are compared.

Table 4.2: Minimum and maximum shear moduli, Young's moduli and Poisson's ratios for the B2 phase [30]

Young's modulus	E_{min} [GPa]	E_{max} [GPa]
	34	131
shear modulus	G_{min} [GPa]	G_{max} [GPa]
	12	48
Poisson's ratio	ν_{min} []	ν_{max} []
	-0.20789	1.0491

Table 4.3: Minimum and maximum Young's moduli, shear moduli and Poisson's ratios for the most energetically stable hydrogen configuration when fully relaxed.

Young's modulus	E_{min} [GPa]	E_{max} [GPa]
	109	189
shear modulus	G_{min} [GPa]	G_{max} [GPa]
	42	71
Poisson's ratio	ν_{min} []	ν_{max} []
	0.1773	0.5294

Table 4.4: Minimum and maximum Young’s moduli, shear moduli and Poisson’s ratios for the most energetically stable hydrogen configuration with only atomic positions relaxed.

Young’s modulus	E_{min} [GPa]	E_{max} [GPa]
	111	235
shear modulus	G_{min} [GPa]	G_{max} [GPa]
	49	90
Poisson’s ratio	ν_{min} []	ν_{max} []
	0.1727	0.64039

Table 4.5: Minimum and maximum Young’s moduli, shear moduli and Poisson’s ratios for a less energetically stable hydrogen configuration with only atomic positions relaxed.

Young’s modulus	E_{min} [GPa]	E_{max} [GPa]
	88	213
shear modulus	G_{min} [GPa]	G_{max} [GPa]
	34	79
Poisson’s ratio	ν_{min} []	ν_{max} []
	0.03	0.74

Table 4.6: Comparison of average bulk modulus, Young’s modulus, shear modulus and Poisson’s ratio calculated using the Voigt scheme for the different configurations.

Phase	B [GPa]	E [GPa]	G [GPa]	ν []
B2 NiTi	160	94	33	0.40222
fully relaxed hydride (lowest energy)	152	151	57	0.33418
partially relaxed hydride (lowest energy)	188	195	74	0.32705
partially relaxed hydride (higher energy)	207	175	64	0.35881

In the following figures, the elastic tensors of the different phases are visualized using the ELATE-tool. It has to be noted that the axis are scaled differently for each structure.

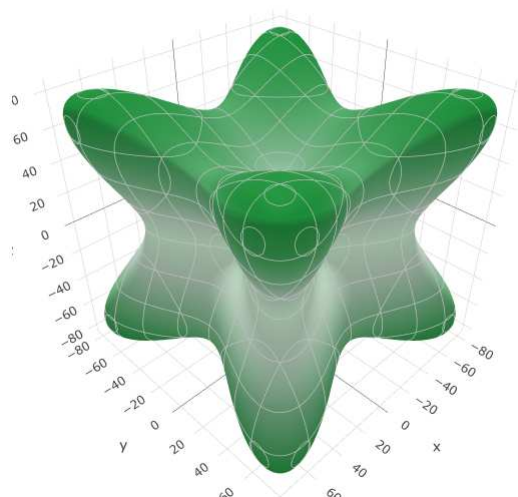


Figure 4.16: Visualized Young's modulus of the B2 phase.

The B2 phase exhibits a very large anisotropy and a low shear modulus.

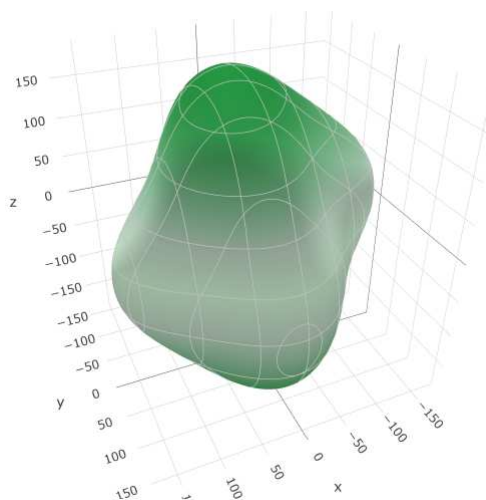


Figure 4.17: Visualized Young's modulus of the fully relaxed hydride with H mostly in Ti planes.

The fully relaxed most energetically stable structure has a significantly smaller anisotropy of all moduli than the B2 phase. The average bulk moduli of the two are comparable, however the hydride in this configuration has a significantly higher average Young's modulus and shear modulus and a lower Poisson's number than the B2 phase.

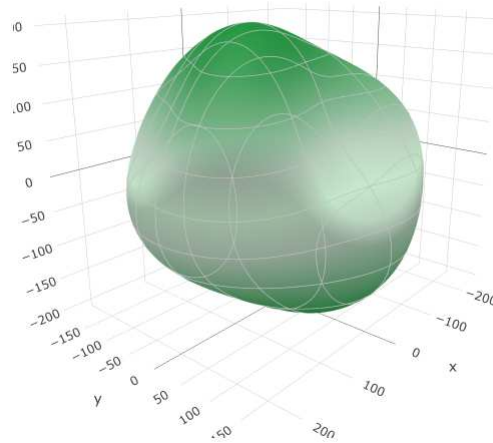


Figure 4.18: Visualized Young's modulus of the partially relaxed hydride with H mostly in Ti planes.

The partially relaxed most energetically stable structure is significantly more rigid than the fully relaxed structure. However, it is also more anisotropic.

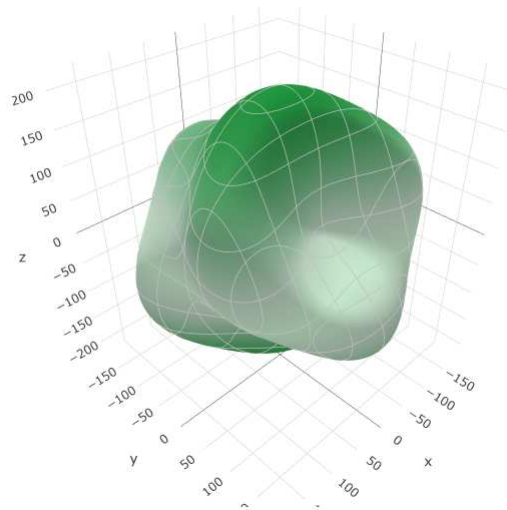


Figure 4.19: Visualized Young's modulus of the partially relaxed hydride with H mostly in Ni planes.

The partially relaxed less energetically stable structure is mechanically stable as opposed to the fully relaxed structure. It is very rigid and has the highest average bulk modulus. The average Poisson's ratio for this configuration is also the closest to that of the B2 phase. Furthermore, the anisotropy is large and close to that of the B2 phase.

Results from the elastic evaluation

There are a few conclusions, which can be drawn from the evaluation of the elastic constants. First of all, it has to be noted that energetic stability and mechanical stability do not perfectly correlate. It is particularly remarkable, that the only partially relaxed structures (which were assumed to be stabilized by the matrix) yield positive eigenvalues, while one of the fully relaxed structures did not yield positive eigenvalues (this might be due to numerical inaccuracies, however the calculation has been repeated with a different strain and yielded the same result). Furthermore, all tested hydride phases are significantly stiffer, have a lower Poisson's ratio and are significantly more isotropic than the matrix. Partially relaxed cells are qualitatively more similar to the B2 phase regarding the anisotropy of elastic constants and Poissons's ratio, however, they are also even stiffer than the fully relaxed cells (with Young's moduli about twice as high). In any case, regardless of the actual structure of the hydride, it can be predicted that it is mechanically a lot stiffer than the matrix.

4.5 Discussion of criteria for phase stability

Based on the observations discussed in the previous sections, the factors, which have been found to influence phase stability are listed in the following:

- The **formation energy number of hydrogen atoms** has a minimum at either two or four hydrogen atoms for all configurations and has a second minimum at around 10 to 16 hydrogen atoms for some configurations.
- The **type of voids occupied** has a significant influence on the phase stability. For almost all structures, the hydrogen atoms relax into octahedral voids in titanium planes (however, as discussed in section 4.3, they are located slightly off-center). Tetrahedral voids have been found to be distinctly unfavorable. A structure with all hydrogen atoms in octahedral voids in nickel planes could be favorable at very high hydrogen contents but further research is needed to confirm this hypothesis.
- The completely relaxed cells with a more distinctly monoclinic **cell shape** tend to be more energetically favorable. An exception here is the structure with artificially clustered hydrogen atoms.
- The **hydrogen distribution** seems to have several effects on the phase stability. First of all, as discussed in section 4.3, clustering of hydrogen atoms has

been found to be less energetically favorable than an equidistant distribution. Furthermore, it has to be noted that the lowest energy structure exhibits some form of additional symmetry of the hydrogen distribution within the cell.

- The evaluation of **mechanical stability** yielded some unexpected mismatch with the energetic stability of unclear origin. What can be definitively said, based on all calculations, however, is that the hydride is likely stiffer and more isotropic than the matrix.

To summarize, the simulations done to determine the phase stability suggest, that a monoclinic structure with twelve hydrogen atoms in octahedral voids of titanium planes is theoretically the most stable atomic structure for the hydride phase, if a stoichiometry of around 33 at.% is assumed. (There would be some other distinctly stable structures at very low amounts of hydrogen for most starting configurations) Furthermore, there is one very energetically favorable structure of $\text{Ni}_{12}\text{Ti}_{12}\text{H}_{16}$ for a random starting configuration. It is not clear, if this structure exhibits an absolute energy minimum as no energies for structures with more than 40 at.% hydrogen have been calculated (this is because for many other configurations, 14 or 16 hydrogen atoms completely disassembled during relaxation, so the cell was assumed to be oversaturated).

Chapter 5

Simulation of confined unit cells

5.1 Equilibrium lattice parameters of partially confined cells

As described in section 4.2, constraints can be put on the relaxation of the cell to more accurately approximate the realistic situation, where the hydride phase is embedded in a B2 matrix. In section 4.2, the constraints used were a completely fixed cell shape and size. To take into account that the surrounding B2 matrix might accommodate changes in the lattice parameters of the hydride phase through fully elastic deformation, the lattice parameters of the hydride phase have been fitted to minimize energy. For simplicity, it is assumed that no shear deformations are possible. This means that the cell angles are fixed at 90° .

The starting configuration used for fitting, is the structure called “H mostly in Ti-planes” with twelve hydrogen atoms (see section 4.1.3). It results in the lowest energy out of all different configurations with this hydrogen content, both when it is fully relaxed and when the cell shape and size are fixed. The already pre-relaxed structure (with fixed cell shape and size) is used as a starting configuration to lower the computational effort.

5.1.1 Dependence on a general scaling parameter

The simplest type of dependence is the one achieved by gradually increasing the volume by elongating the basis vectors of the unit cell, keeping the ratio between them consistent.

The results from this fit are shown in figures 5.1 to 5.4.

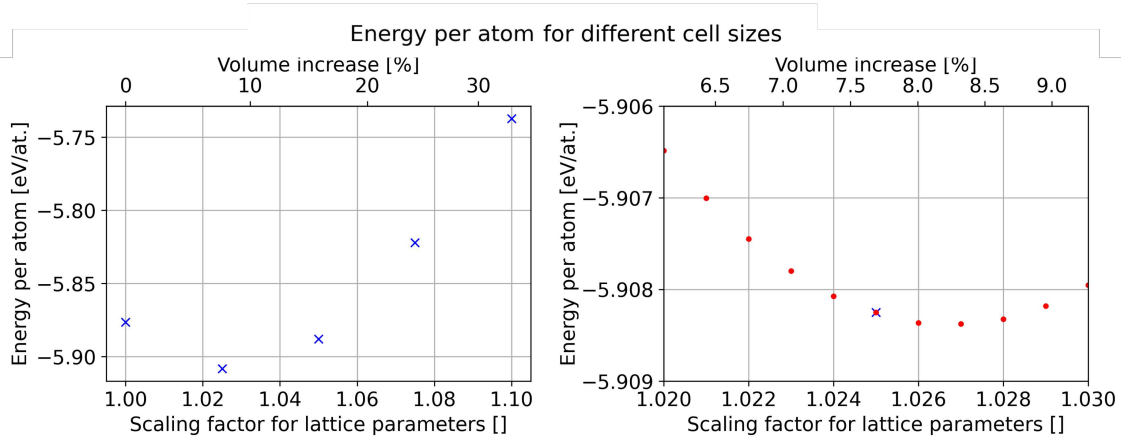


Figure 5.1: Energy per atom for a coarse fit up to a 10% length increase (left) and values at 0.1% intervals around the minimum at 2.5% (right).

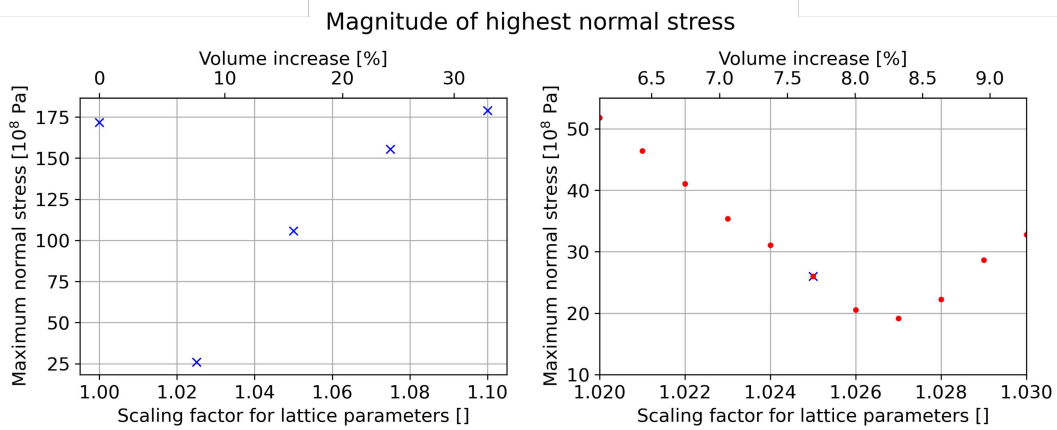


Figure 5.2: Magnitude of highest normal stress (evaluated for each data point, so it is not always the same stress component) for a coarse fit up to a 10% length increase (left) and values at 0.1% intervals around the minimum at 2.5% (right).

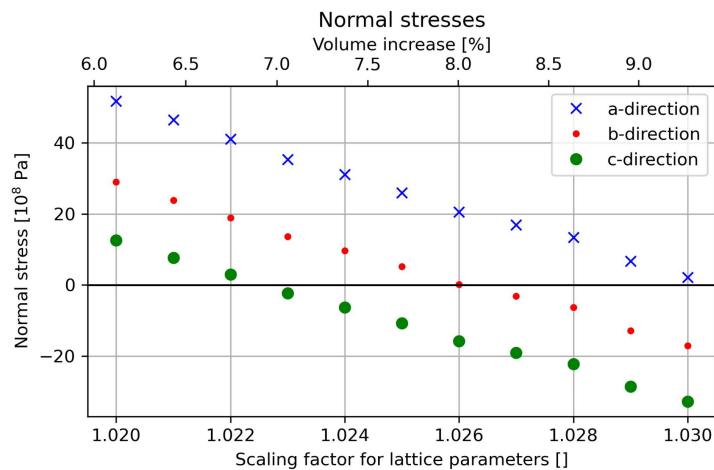


Figure 5.3: Normal stresses for different cell sizes.

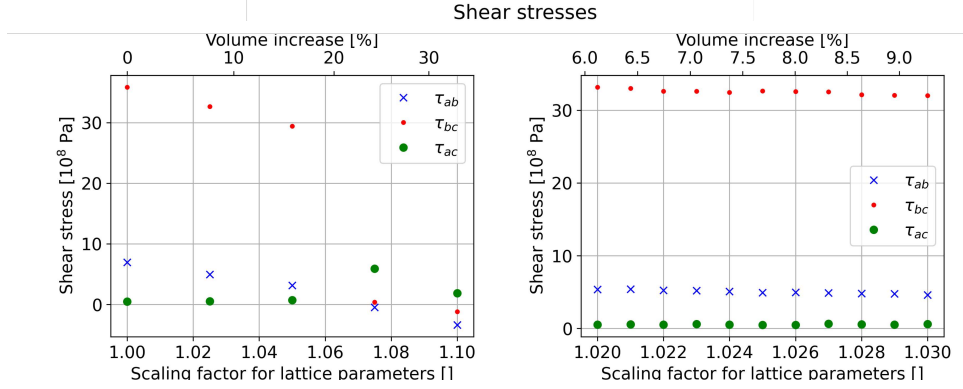


Figure 5.4: Shear components of the stress tensor over the scaling parameter for the coarse fit up to a 10% length increase (left) and values at 0.1% intervals around the minimum at 2.5% (right).

The coarse fit at intervals of 2.5% from 100% to 110% of each lattice parameter shows a minimum in energy in the vicinity of a length increase to 102.5%. Further calculations have thus been performed for scaling factors from 102% to 103% in increments of 0.1%. There is a clear energy minimum at a length scaling factor between 102.6% and 102.7%, as shown in figure 5.1, which corresponds to a volume increase of 8.16% (taking 102.65% as the linearly interpolated value).

While there is a clear energy minimum, it has to be noted, that not all stresses are relaxed. This is depicted in figure 5.2 which shows that even for the most energetically stable configurations, there are residual stresses up to $20 \cdot 10^8$ Pa. Figure 5.3 gives insight into this observation by individually showing the dependence of the stresses in different directions on the scaling parameter. At the most energetically stable cell size, only the stresses in the b -direction are fully relaxed while there are tensile stresses in the a -direction and compressive stresses in the c -direction still present (The highest stress magnitude in this case is the tensile stress in the a -direction — represented by the datapoint in figure 5.2). This leads to the assumption that the ratio between the three lattice parameters would have to change in order to reach a lower energy state.

Looking at the shear stresses in figure 5.4, there is no minimum around the energetically most stable structure and τ_{bc} remains at a value of over $30 \cdot 10^8$ Pa. This is to be expected as the evaluated configuration would transform into a monoclinic shape, if the angles were relaxed into their equilibrium state (see section 4.1.3). However, figure 5.4 also displays a sudden decrease in shear stress at very large cell sizes that are distinctly energetically unfavorable. This unexpected observation is further explored in section 5.2.

5.1.2 Individually fitted lattice parameters

As discussed in section 5.1.1, there is no complete relaxation of all stresses if the cell is scaled equiaxially. This is why a second fit has been performed where the cell parameters are changed independently from each other. This will give insight into how the lattice parameters change relative to each other when the cell is embedded into an anisotropically compressible matrix. The first sets of scaling parameters have been chosen manually based on the results from the previous fit.

The energetically most favorable structure (which can be assumed to be the one with the lowest residual stresses due to the fact that the starting configurations used are identical apart from the scaling parameters) is one where a is increased by 3.5%, b is increased by 2.5% and c is increased by 1.5%. This also matches the zero crossing of the different stresses in 5.4 decently.

The relaxed structure with these cell parameters has been used as a starting configuration for a relaxation using the Gadget code [36]. Gadget makes it possible to put more specific constraints on the structural relaxation than VASP — in this case keeping the angles at 90° . The results from this fit are listed in table 5.1.

Table 5.1: Initial (unrelaxed) lattice parameters and their corresponding scaled equilibrium lattice parameters.

Lattice parameter	initial length [\AA]	increase [%]	optimized length [\AA]
a	8.505	4.11	8.855
b	7.366	2.50	7.550
c	5.208	1.25	5.273

The total increase in cell size using these fitted parameters is 8.05%, which is very close to the 8.16% resulting from the first fit described in section 5.1.1. This can be seen as the equilibrium size increase of the cell due to the addition of twelve hydrogen atoms, which needs to be accounted for in some way (residual stresses or straining of the matrix) when the hydride is embedded into a B2 matrix.

5.2 Phase change upon scaling confined cells

As mentioned in section 5.1.1 and shown in figure 5.4, if the cell parameters are scaled to 107.5%, an unexpected change in stresses can be observed. More cells of different sizes (with scaling parameters between 1.05 and 1.075 where the sudden decrease occurs) have thus been relaxed in order to better quantify when the change occurs.

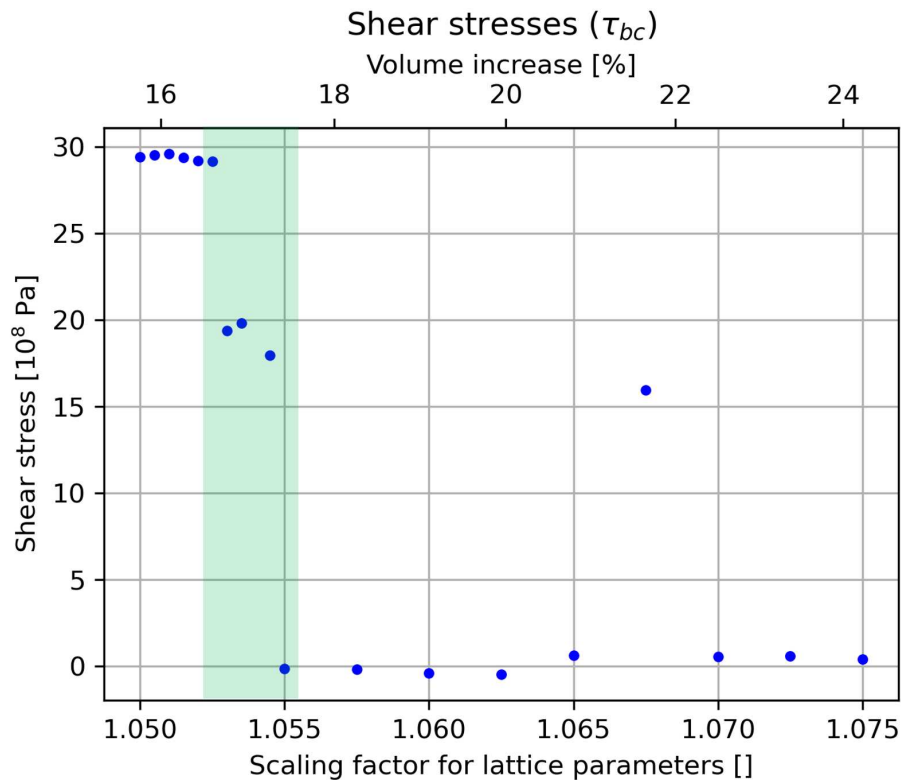


Figure 5.5: Shear stress component τ_{bc} over the scaling parameter for lattice parameter, showing abrupt changes in stresses for certain cell sizes (area of interest marked in green).

As shown above, the decrease in stresses happens in two steps, one between 5.25% and 5.30% increase and one between 5.45% and 5.50%. It also has to be noted, that the relaxation of a structure with lattice parameters increased by 5.40% yielded no result since the calculation did not converge. Furthermore, there is an increase in stress for lattice parameters increased by 6.75%. The following figures show the actual differences in atomic positions between the structures where a change in stresses occurs.

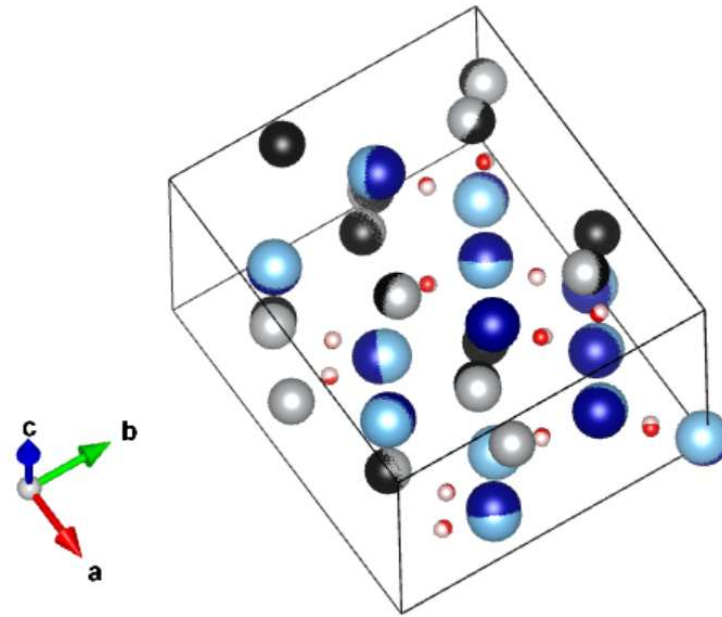


Figure 5.6: Comparison of relaxed structures for an increase of lattice parameters of 5.525% (dark colors) and 5.535% (light colors).

The figure above depicts the comparison between a structure that shows the expected behavior (5.525% which has relatively high residual shear stresses) and a structure which exhibits the first decrease in energy as shown in figure 5.5 (5.535%). While there is a clear shift in some atomic positions beyond what is expected simply due to the increase in cell size, there is no qualitative difference in hydrogen distribution and the same octahedral voids are occupied.

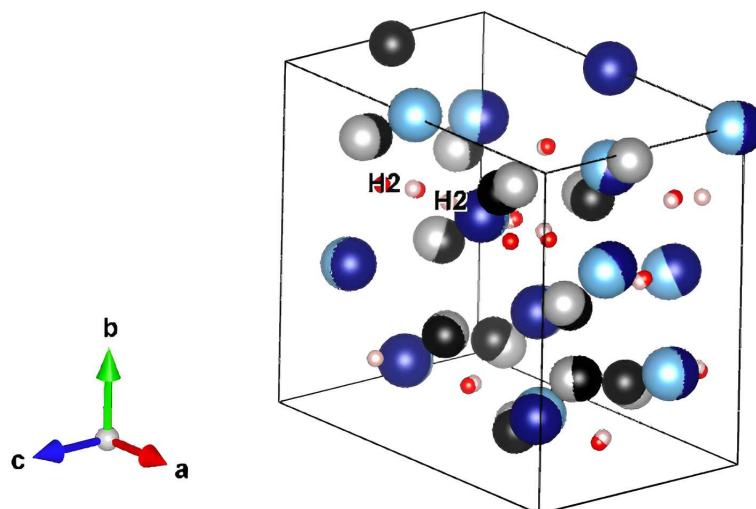


Figure 5.7: Comparison of relaxed structures for an increase of lattice parameters of 5.535% (dark colors) and 5.550% (light colors).

In figure 5.7 the structure with a 5.535% increase in lattice parameters is compared to a structure with an increase of 5.550% which has negligible residual shear components. In figure 5.7, hydrogen atom H2 is marked in both configurations to emphasize the fact that it relaxed into a different position for the different cell sizes, even though the starting configuration is qualitatively the same. It has to be noted, that in both cases H2 relaxes into an octahedral void in Ti-planes, but for the larger structure it migrates away from the starting position into a different void.

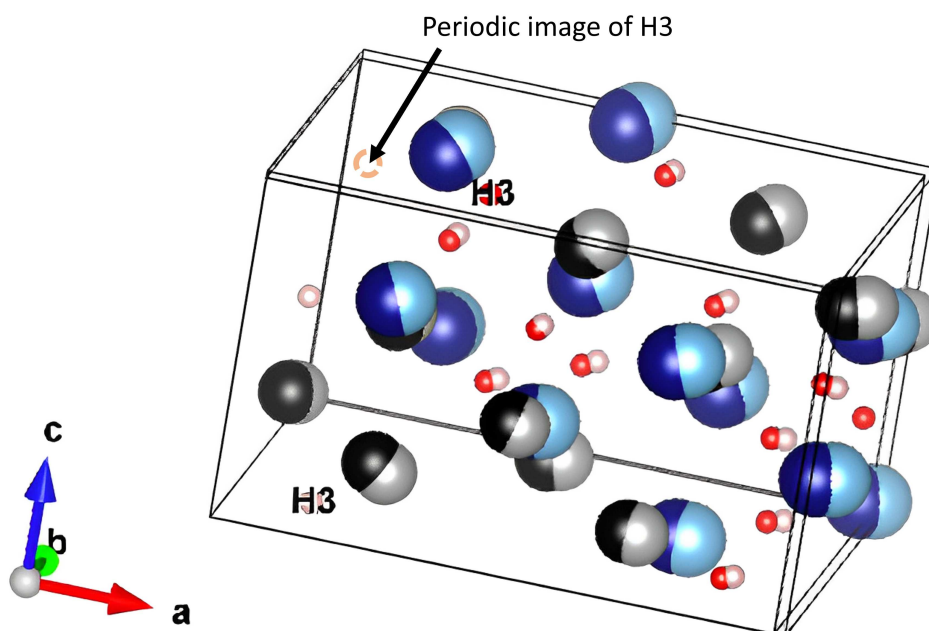


Figure 5.8: Comparison of relaxed structures for an increase of lattice parameters of 5.550% (dark colors) and 7.50% (light colors).

When comparing the structure at a 5.50% increase and a 7.50% increase in lattice parameters (see figure 5.8), while the shear stresses are very comparable, qualitatively, there is a difference in the position hydrogen atom H3 which occupies as different octahedral void.

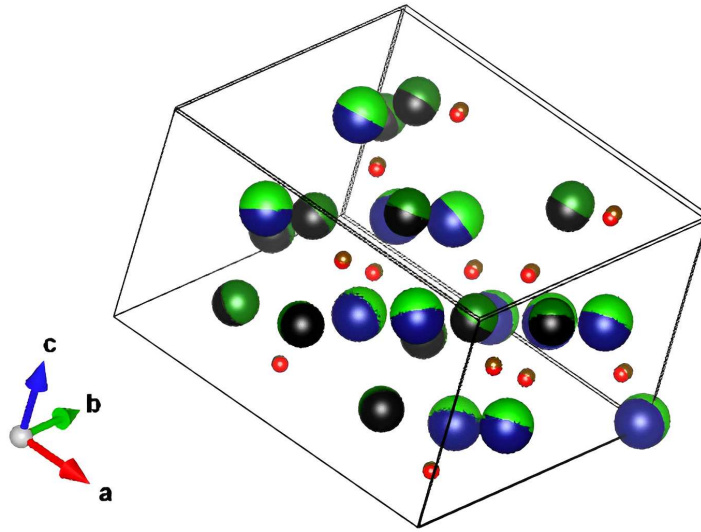


Figure 5.9: Comparison of relaxed structures for an increase of lattice parameters of 5.535% (dark colors) and 6.750% (green and brown atoms).

When examining the plot in figure 5.5, a sudden increase of shear stresses for the structure with an increase in lattice parameters of 6.75% is immediately noticeable. This structure is compared to one with a 5.35% increase which has a similar shear stress magnitude in figure 5.9. When looking at the hydrogen positions, the structure with an 6.75% increase has the same hydrogen distribution as the structure at a 5.35% increase. In the following section, the energies of the different structures will be compared, in order to find a possible explanation for this change in positions.

5.2.1 Possible explanation for the change in stresses

As a conclusion of the analysis of the relation between shear stresses and hydrogen distribution, it can be said that a sudden large decrease in shear stresses can correspond to a redistribution of a few hydrogen atoms. This is particularly remarkable, because the starting configuration for the relaxation already had hydrogen atoms placed in the positions expected to be the most stable. In order for this change to occur, the hydrogen atoms must move from one octahedral void to a different octahedral void during the relaxation process.

One possible explanation for the change in structure arises from the energy per atom plotted in figure 5.10 over the increase in lattice parameters.

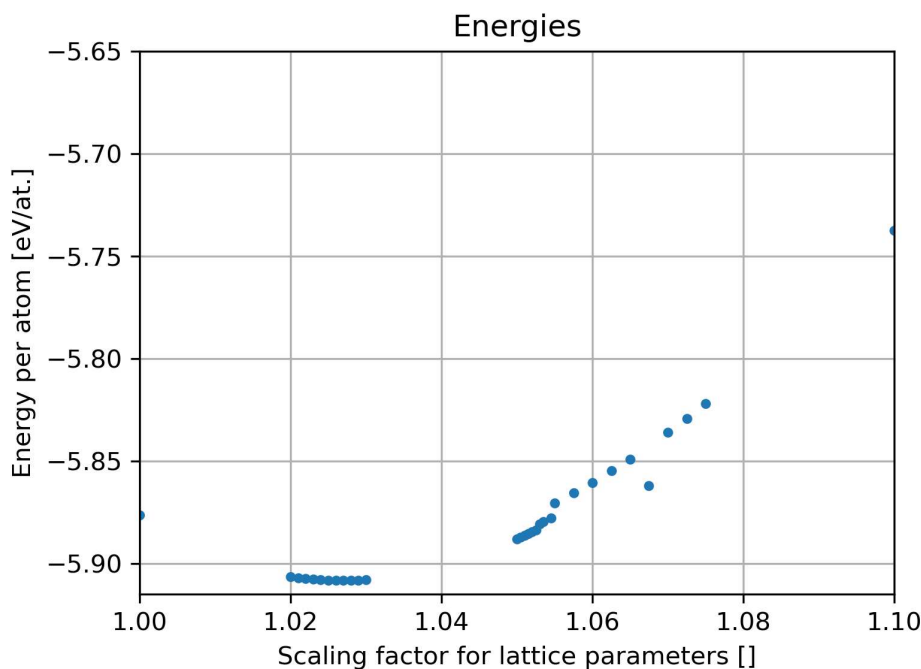


Figure 5.10: Energies per atom for all relaxed structures.

There is a clear jump in energy between the structures with higher and lower shear stresses. In addition higher shear stresses generally correspond to lower energy states. This also supports the observation discussed in section 4.2, that fully relaxed cells with a greater monoclinic angle are more energetically favorable. Three energy curves can be very coarsely fitted (using a quadratic fit), corresponding to the three different hydrogen configurations discussed in section 5.2. The result is shown in figure 5.11. It should be noted that the outlier at 6.75% fits none of the energy curves.

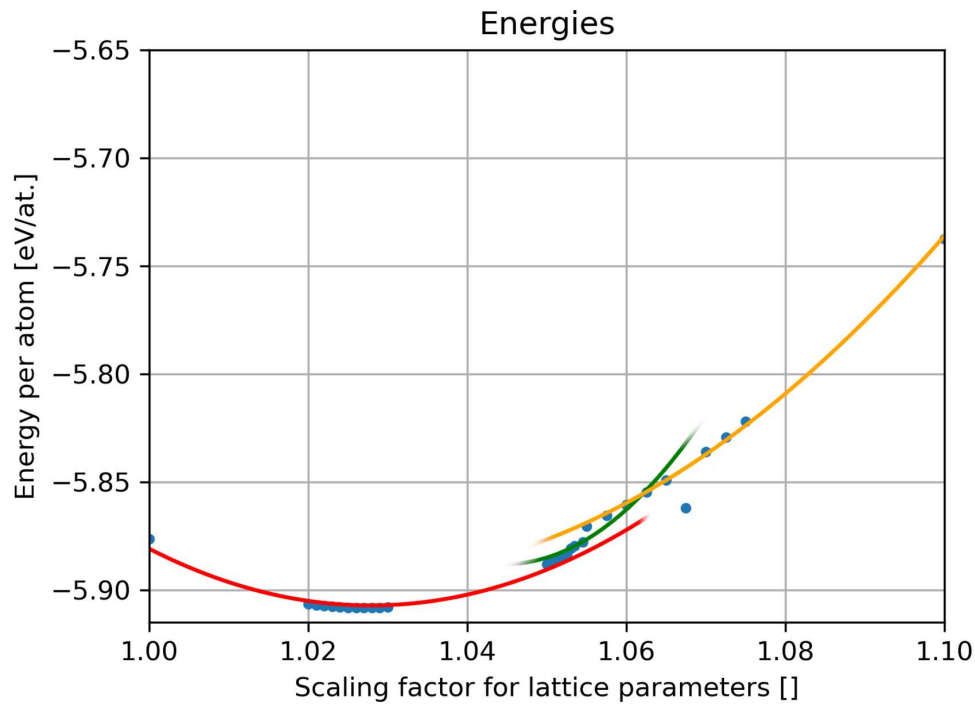


Figure 5.11: Energies per atom for all relaxed structures.

Figure 5.11 suggests, that the configurations with lower shear stresses correspond to energetically more unfavorable states. A relaxation into these configurations which exhibit low shear stresses (see figure 5.4) would thus be metastable. This hypothesis is supported by the fact that there is one data point where the system relaxes into a significantly more stable structure with higher shear stresses (at an increase of 6.75%). Why exactly this lower energy state is not reached and what its energy curve might look like are open questions that demand further investigation in the future.

Chapter 6

Discussion of diffraction patterns

6.1 Effect of hydrogen distribution on diffraction patterns

It has been experimentally shown by Dlouhý and colleagues that there is a difference between the diffraction patterns of pure NiTi and a NiTi hydride phase embedded into the matrix. The diffraction pattern of the hydride phase has been used to create the orthorhombic unit cell, which is the starting point for the calculations extensively discussed in the previous sections. The experimentally found diffraction pattern is depicted in figure 2.12.

In order to further assess the reliability of the results from the previous sections, the diffraction patterns for some of the most stable structures which were created have been simulated using the “Dans diffraction” Python package [39]. A link to the code used to simulate the diffraction patterns can be found in the appendix. Good agreement between the measured and simulated diffraction patterns would indicate that the simulated structure is very similar to the one found experimentally.

6.1.1 Comparison of diffraction patterns

In the following, different diffraction patterns simulated with the “Dans diffraction” package are compared. The simulated zone axis is always (001) with no displacement from the origin. The colorscale on the right represents intensity in arbitrary units and is simply manipulated to scale the intensity of all spots. The relative intensity of a spot is also represented by its size.

Diffraction pattern of the B2 matrix without hydrogen

The diffraction pattern of the B2 matrix is shown in figure 6.1.

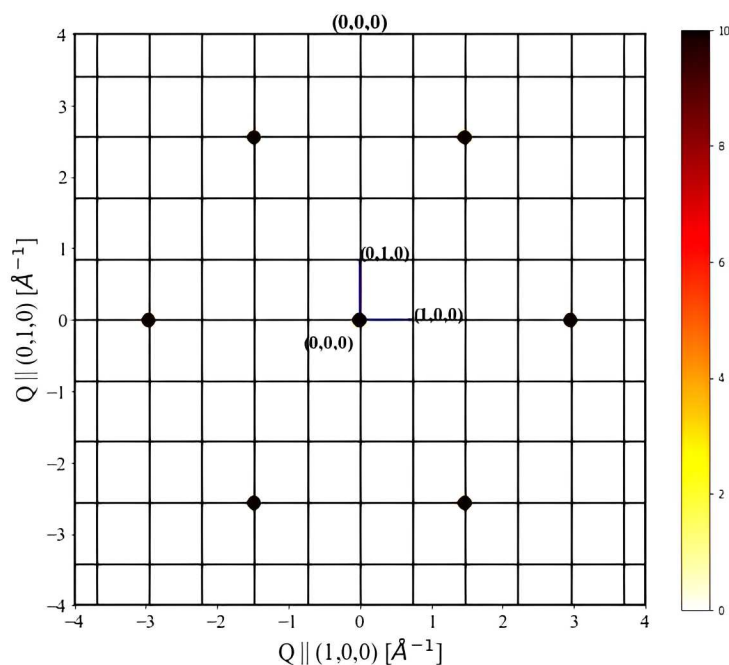


Figure 6.1: Diffraction pattern of the B2 matrix.

In the measured diffraction pattern, the spots present in this simulated pattern are the brightest (see figure 2.12).

Unrelaxed structure

The structure, which was found to be most stable in chapter 4 when relaxed has been used in its **unrelaxed** state to simulate a diffraction pattern. The result is shown in figure 6.2. Quite remarkably, the addition of hydrogen atoms into the tetrahedral voids of the cell causes only a very small change in the resulting diffraction pattern. In figure 6.3, the additional diffraction spots are shown by lowering the threshold

for detection of spots by 4 orders of magnitude. What is notable about this pattern is that there are no spots directly along the (100) axis present like they are in the measured pattern (see figure 2.12).

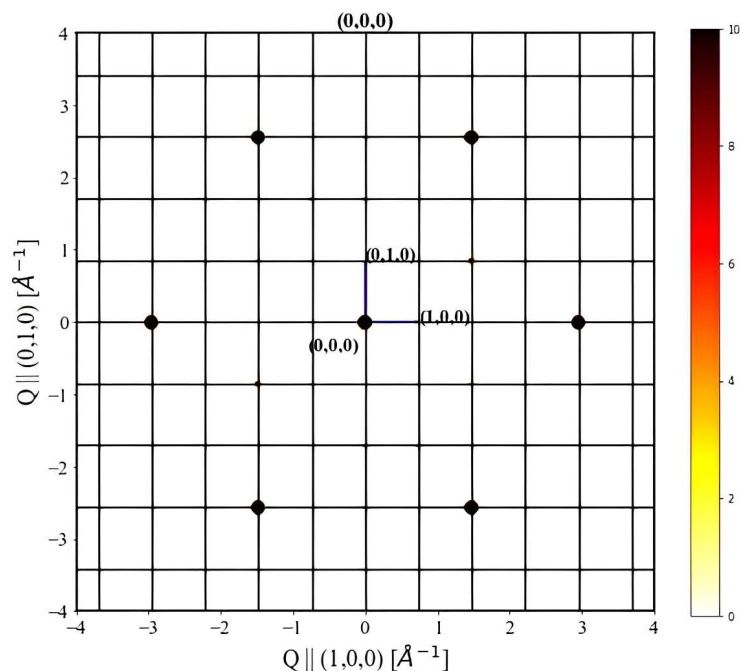


Figure 6.2: Diffraction pattern of the unrelaxed structure with hydrogen placed in tetrahedral voids.

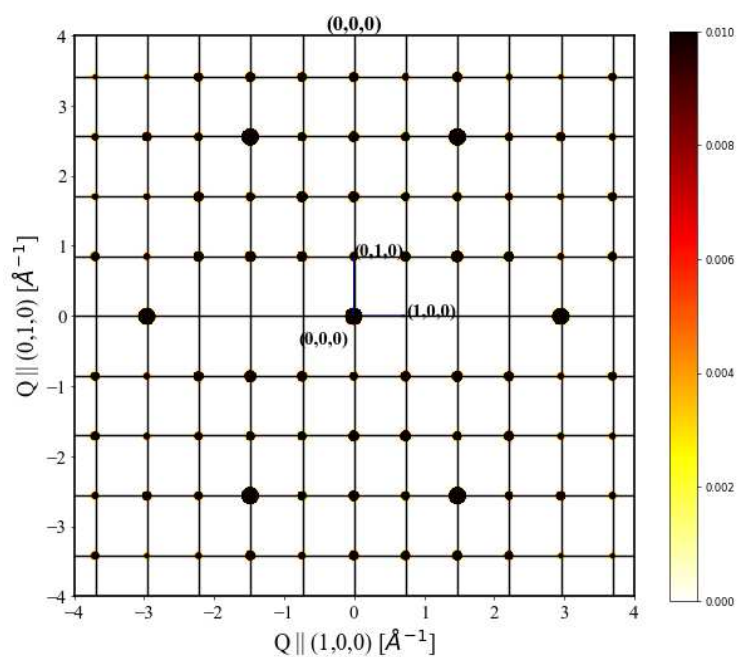


Figure 6.3: Diffraction pattern of the unrelaxed structure with hydrogen placed in tetrahedral voids; detection threshold 10^{-4} times smaller than in figure 6.1.

Relaxed structures

For the diffraction pattern in figure 6.4, the structure from section 6.1.1 has been relaxed completely, both in shape and atomic positions.

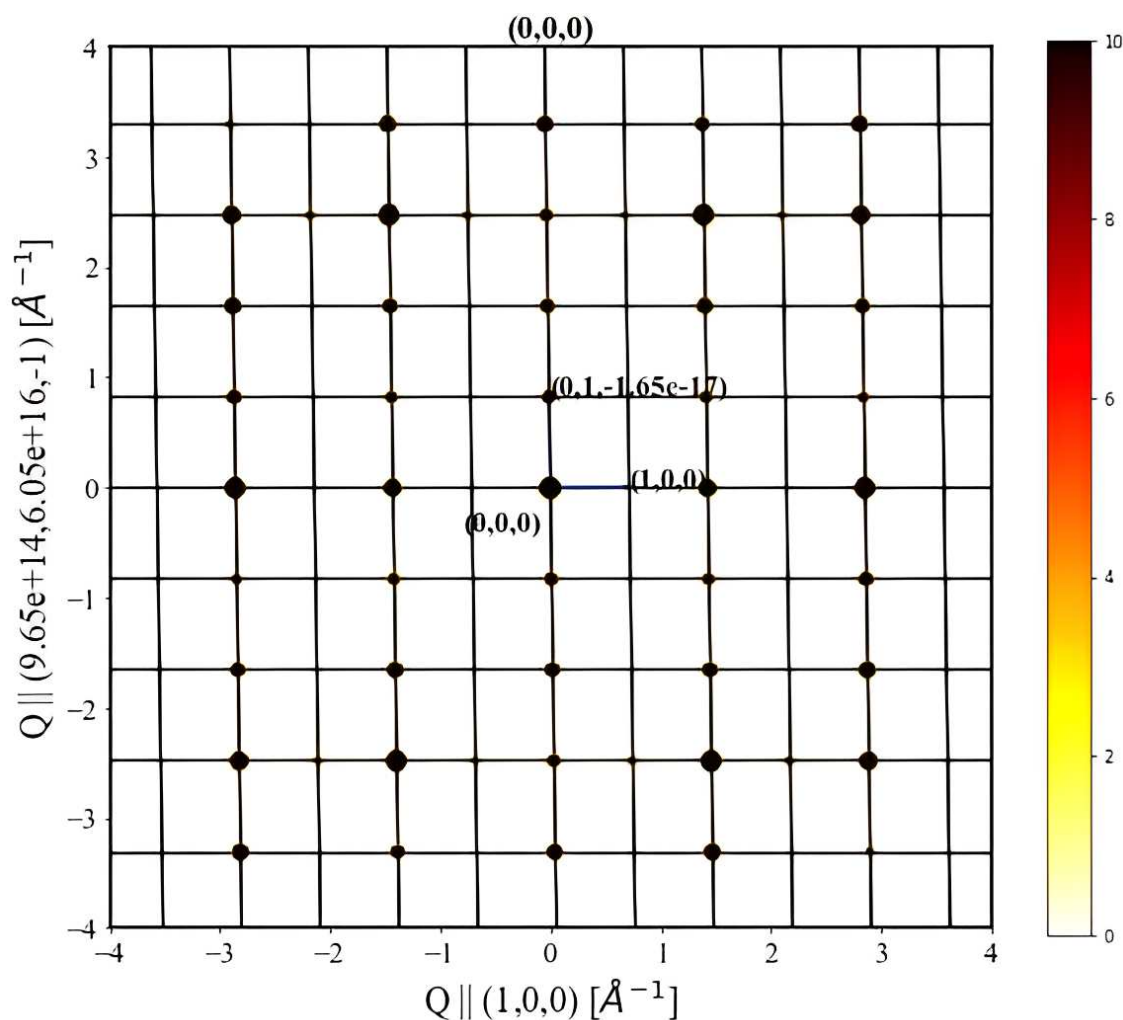


Figure 6.4: Diffraction pattern of the completely relaxed structure.

The resulting pattern qualitatively agrees with the experimentally observed pattern shown in figure 2.12. (It has to be noted that due to the change in cell shape, the y -axis of the plot very slightly changed) Now, there are very clearly visible diffraction spots along the (100)-axis, which suggests that they are caused either by hydrogen atoms in octahedral voids or by displacing the lattice atoms (since they were not present in the unrelaxed structure with hydrogen in tetrahedral voids).

Figure 6.5 shows the resulting diffraction pattern when the structure is **completely confined in the matrix** (fixed cell shape).

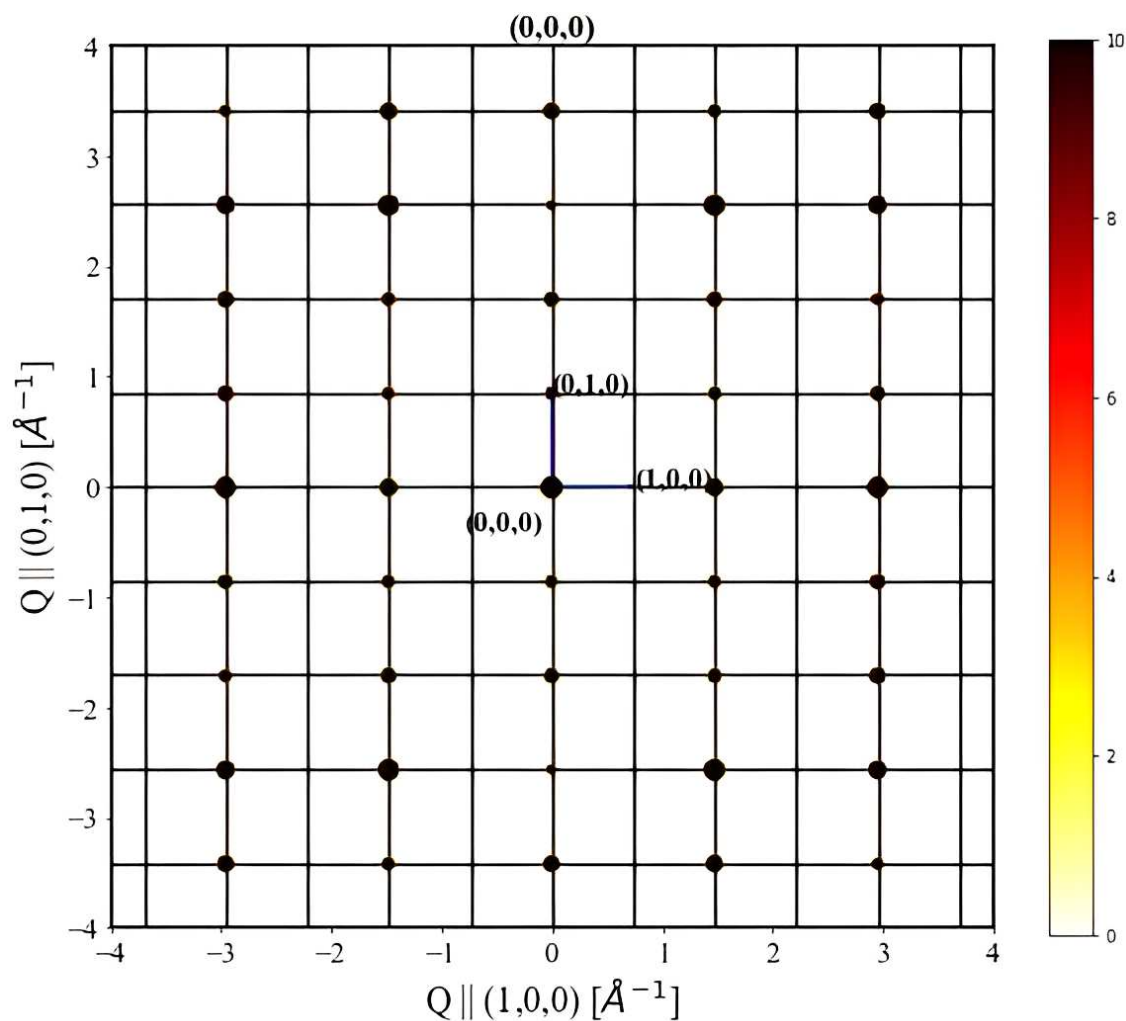


Figure 6.5: Diffraction pattern of the relaxed structure with fixed cell shape and size.

The resulting diffraction pattern is almost identical to both the measured pattern and the pattern of the completely relaxed cell. (figure 6.4) This suggests that the cell shape has significantly less influence on the diffraction pattern than the atomic positions.

Diffraction pattern of relaxed structures with hydrogen removed

It was shown in section 6.1.1 that for an unrelaxed structure, hydrogen atoms themselves have a negligible contribution to the diffraction pattern. In figure 6.6, the diffraction patterns of the relaxed structures with 12 hydrogen atoms from section 6.1.1 (figure 6.4) are compared to the diffraction patterns of the same relaxed structures, but with the hydrogen atoms removed after relaxation. All nickel and titanium atoms remain fixed in their positions after removal of hydrogen atoms.

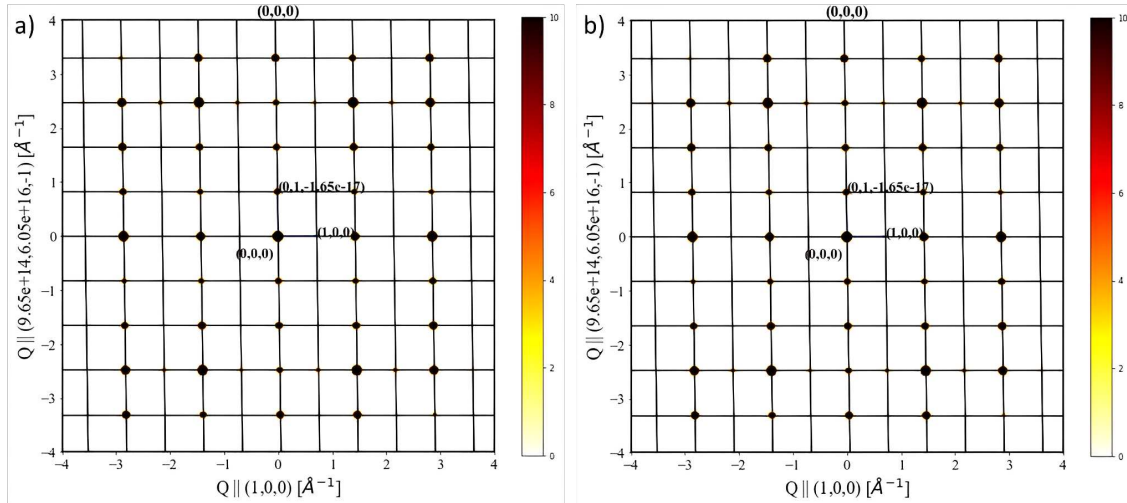


Figure 6.6: (a) Diffraction pattern of the fully relaxed structure with hydrogen atoms (also shown in figure 6.4); (b) diffraction pattern of the fully relaxed structure with hydrogen atoms removed.

The fact that the two diffraction patterns are almost indistinguishable at the applied scale speaks for the hypothesis, that the most important factor influencing the diffraction pattern is the shift of nickel and titanium atoms due to the presence of hydrogen and not the hydrogen atoms themselves.

6.1.2 Summary of observations

An especially interesting result from this evaluation is that there is almost no discernible difference between structures with hydrogen atoms present in the cell and relaxed structures with hydrogen removed. It is also remarkable how similar *all* shown diffraction patterns of relaxed structures with interstitial hydrogen are. This even applies to the few structures where hydrogen relaxes into tetrahedral voids corresponding to a higher energy state; however, an unrelaxed structure with hydrogen only in tetrahedral voids, such as the one shown in figure 6.2, does not match the experimentally found diffraction pattern.

A possible explanation for why the diffraction patterns are very similar for all relaxed structures might be, that the additional diffraction spots are mainly caused by the shift of nickel and titanium atoms. This would mean that the diffraction pattern of the phase gives little insight into actual hydrogen distribution, but also that none of the structures relaxed in chapter 4 can be excluded due to not matching the diffraction pattern.

Chapter 7

Closing remarks and outlook

7.1 Closing remarks

The findings discussed in sections 4.5 and 6.1.2 help to characterize the hydride phase, which was experimentally discovered in NiTi. The results of this assessment include the predicted structural and mechanical properties of the phase as well as the simulated diffraction patterns. This evaluation is however incomplete in the sense, that only hand-picked structures with very specific characteristics have been simulated and compared. To gain a more clear picture, an extensive statistical evaluation of the hydrogen distribution and chemical potential of a significantly larger number of structures would need to be performed. This lies outside the scope of this work, however the evaluation methods used in this thesis will lay a solid groundwork for future research.

Furthermore, section 5.2.1 summarizes the findings regarding a possible phase change if the unit cell of the hydride is scaled up. This effect is not described in literature and even though it is unclear if it has any practical application, it warrants further investigations to gain a more thorough theoretical understanding of the stability of the NiTi hydride phase.

The findings discussed in section 6.1.2 suggest, that the simulation of diffraction patterns does not give clear insight into the chemical composition of the material, because the change in diffraction is mainly caused by shifting of the lattice atoms and relatively independent of the hydrogen concentration. They can, however, be used to exclude a few structures that do not fit the pattern at all.

7.2 Outlook

In order to continue the evaluation of the phase stability, a statistical evaluation will be performed in the future, using “energetically favorable starting configurations” which have been created using the Monte Carlo method. Since it has been found that diffraction patterns give little insight into chemical composition, it would be worthwhile to try different evaluation methods to gain insight into the stoichiometry and structure of the hydride phase. Another open question which warrants further investigation is, why the relaxation of one configuration of $\text{Ni}_{12}\text{Ti}_{12}\text{H}_{16}$ resulted in a very energetically stable structure with hydrogen in nickel planes, which neither agrees with past research (see Ref. [31]) nor with the general pattern found in this work.

Bibliography

- [1] T. Duerig, A. Pelton, and D. Stöckel. “The Use of Superelasticity in Medicine”. In: *Metall* 50 (Sept. 1996).
- [2] D. Stoeckel, A. Pelton, and T. Duerig. “Self-expanding nitinol stents: material and design considerations”. In: *Eur. Radiol.* 14.2 (Feb. 2004), pp. 292–301.
- [3] Jack McLure. *Stent*. [Online; accessed February 14, 2023]. URL: <https://creativecommons.org/licenses/by-sa/4.0/deed.en>.
- [4] C. Song. “History and Current Situation of Shape Memory Alloys Devices for Minimally Invasive Surgery”. In: *Open Med Dev J* 2 (Feb. 2010), pp. 24–31. DOI: [10.2174/1875181401002020024](https://doi.org/10.2174/1875181401002020024).
- [5] S. Alipour et al. “Nitinol: From Historical Milestones to Functional Properties and Biomedical Applications”. In: *Proceedings of the Institution of Mechanical Engineers Part H Journal of Engineering in Medicine* (Sept. 2022). DOI: [10.1177/09544119221123176](https://doi.org/10.1177/09544119221123176).
- [6] J. Aragon, J. Villada, and J. Ruiz-Moreno. “Ocular Biocompatibility of a Nitinol Capsular Tension Ring (CTR)”. In: *The EuroBiotech Journal* 6 (Oct. 2022), pp. 167–173. DOI: [10.2478/ebtj-2022-0016](https://doi.org/10.2478/ebtj-2022-0016).
- [7] M.J. Mahtabi, N. Shamsaei, and B. Rutherford. “Mean Strain Effects on the Fatigue Behavior of Superelastic Nitinol Alloys: An Experimental Investigation”. In: *Procedia Engineering* 133 (Dec. 2015), pp. 646–654. DOI: [10.1016/j.proeng.2015.12.645](https://doi.org/10.1016/j.proeng.2015.12.645).
- [8] J.G. Lee. *Computational Materials Science: An Introduction*. Taylor & Francis, 2011.
- [9] D. Holec. *Lecture notes in Solid State Physics*. Apr. 2021.
- [10] VASP. *Symmetry and sampling in reciprocal space / VASP Lecture*. [Online; accessed January 11, 2023]. 2022. URL: <https://www.youtube.com/watch?v=rvGwCdQE07Q>.

- [11] G. Kresse and J. Hafner. “Ab initio molecular dynamics for liquid metals”. In: *Phys. Rev. B* 47 (1 Jan. 1993), pp. 558–561. DOI: [10.1103/PhysRevB.47.558](https://doi.org/10.1103/PhysRevB.47.558).
- [12] G. Kresse and D. Joubert. “From ultrasoft pseudopotentials to the projector augmented-wave method”. In: *Phys. Rev. B* 59 (3 Jan. 1999), pp. 1758–1775. DOI: [10.1103/PhysRevB.59.1758](https://doi.org/10.1103/PhysRevB.59.1758).
- [13] G. Kresse and J. Furthmüller. “Efficiency of ab-initio total energy calculations for metals and semiconductors using a plane-wave basis set”. In: *Comput. Mater. Sci.* 6.1 (July 1996), pp. 15–50.
- [14] G. Kresse and J. Furthmüller. “Efficient iterative schemes for ab initio total-energy calculations using a plane-wave basis set”. In: *Phys. Rev. B Condens. Matter* 54.16 (Oct. 1996), pp. 11169–11186.
- [15] K. Momma and F. Izumi. “VESTA: A Three-Dimensional Visualization System for Electronic and Structural Analysis”. In: *Journal of Applied Crystallography - J APPL CRYST* 41 (June 2008), pp. 653–658. DOI: [10.1107/S0021889808012016](https://doi.org/10.1107/S0021889808012016).
- [16] VASP. *Available PAW potentials*. [Online; accessed January 12, 2023]. 2022. URL: https://www.vasp.at/wiki/index.php/Available_PAW_potentials#Recommended_potentials_for_DFT_calculations.
- [17] C. Mitterer. *Lecture on Functional Materials*. Oct. 2021.
- [18] D.C. Lagoudas. *Shape Memory Alloys: Modeling and Engineering Applications*. Springer ebook collection / Chemistry and Materials Science 2005-2008. Springer US, 2008.
- [19] J. Perkins, ed. *Shape Memory Effects in Alloys*. Springer US, 1975. DOI: [10.1007/978-1-4684-2211-5](https://doi.org/10.1007/978-1-4684-2211-5).
- [20] K. Otsuka and X. Ren. “Physical metallurgy of Ti–Ni-based shape memory alloys”. In: *Prog. Mater. Sci.* 50.5 (July 2005), pp. 511–678.
- [21] M. Fouda, M. Tawfik, and G. M. El-Bayoumi. “Calibration of The Hysteresis Loop of SMA Wires Heated by Electric Current”. In: May 2012. DOI: [10.13140/2.1.2237.7286](https://doi.org/10.13140/2.1.2237.7286).
- [22] Mmm-jun. “Schematic demonstration of the shape memory effect in alloys”. [Online; accessed January 11, 2023]. PhD thesis. URL: <https://creativecommons.org/licenses/by-sa/4.0/deed.en>.
- [23] I. Shishkovsky. “Functional design of porous drug delivery systems based on laser assisted manufactured nitinol”. In: vol. 1415. Nov. 2011. DOI: [10.1557/opl.2012.3](https://doi.org/10.1557/opl.2012.3).

- [24] H. Hsiao et al. “A novel nitinol spherical occlusion device for liver cancer”. In: *Materials (Basel)* 9.1 (Jan. 2016), p. 19.
- [25] J. C. K. Fong. *Wireless MEMS drug delivery device enabled by a micromachined Nitinol actuator as a pumping mechanism*. 2014.
- [26] L. Yahia. *Shape Memory Polymers for Biomedical Applications*. Elsevier Science, 2015.
- [27] Doomgiver. “Binary phase diagram of NiTi with nitinol’s range”. In: (2012). [Online; accessed February 13, 2023]. URL: <https://creativecommons.org/licenses/by-sa/3.0?ref=openverse>.
- [28] Tomduerig. *Nitinol Ms vs Ni content*. [Online; accessed January 11, 2023]. URL: https://upload.wikimedia.org/wikipedia/commons/thumb/0/0f/Nitinol_Ms_vs_Ni_content.jpg/676px-Nitinol_Ms_vs_Ni_content.jpg?20091004231757.
- [29] M. Kaack. “Elastische Eigenschaften von NiTi-Formgedächtnis-Legierungen”. doctoralthesis. Ruhr-Universität Bochum, Universitätsbibliothek, 2003.
- [30] Candida S. Punla et al. “Are we there yet?: An analysis of the competencies of BEED graduates of BPSU-DC”. In: *International Multidisciplinary Research Journal* 4.3 (Sept. 2022), pp. 50–59.
- [31] D. Holec et al. “Ab initio study of point defects in NiTi-based alloys”. In: *Physical Review B* 89 (Oct. 2013). DOI: [10.1103/PhysRevB.89.014110](https://doi.org/10.1103/PhysRevB.89.014110).
- [32] J. L. Soubeyroux et al. “Structural study of the hydrides NiTiH_x ($x = 1.0$ and 1.4)”. In: *J. Alloys Compd.* (1993). ISSN: 0925-8388.
- [33] T. Ogawa et al. “Hydrogen embrittlement behavior of Ni-Ti shape memory alloy with different microstructures in acidic fluoride solution”. In: *International Journal of Mechanical and Materials Engineering* 10.1 (July 2015), p. 12.
- [34] J. Sheriff, A. Pelton, and L. Pruitt. “Hydrogen Effects on Nitinol Fatigue”. In: *Medical Device Materials II - Proceedings of the Materials and Processes for Medical Devices Conference 2004* (Jan. 2006).
- [35] Jr. Eggers D.F. et al. *Physical Chemistry*. Wiley, John Sons, 1964.
- [36] T. Bucko, J. Hafner, and J. Angyán. “Geometry optimization of periodic systems using internal coordinates”. In: *J. Chem. Phys.* 122.12 (Mar. 2005), p. 124508. DOI: [10.1063/1.1864932](https://doi.org/10.1063/1.1864932).

- [37] R. Yu, J. Zhu, and HQ. Ye. “Calculations of single-crystal elastic constants made simple”. In: *Comput. Phys. Commun.* 181.3 (Mar. 2010), pp. 671–675. DOI: [10.1016/j.cpc.2009.11.017](https://doi.org/10.1016/j.cpc.2009.11.017).
- [38] R. Gaillac, P. Pullumbi, and F.X. Coudert. “ELATE: an open-source online application for analysis and visualization of elastic tensors”. In: *Journal of Physics: Condensed Matter* 28.27 (May 2016), p. 275201. DOI: [10.1088/0953-8984/28/27/275201](https://doi.org/10.1088/0953-8984/28/27/275201).
- [39] D. Porter. *Dans Diffraction python package*. URL: <https://pypi.org/project/DansDiffraction/> (visited on 01/08/2023).

.1 Python scripts

The code used to calculate interatomic distances and to simulate diffraction patterns has been released on GitHub under the following link:

<https://github.com/AnnaPaulik/NiTiHevaluation/releases/tag/structureEvaluation>

.2 Calculation parameters

.2.1 For atomic fcc nickel

INCAR:

ENCUT = 450

IBRION = 2

ISIF = 3

LCHARG = False

LWAVE = False

NCORE = 2

NSW = 100

with the PAW_PBE Ti potential and 15x15x10 k -points. Lattice parameters were taken from the materials project website [30].

.2.2 For atomic hcp titanium

INCAR:

```
ISIF = 3
ISPIN = 2
LCHARG = False
LWAVE = False
MAGMOM = 4*2.0
NCORE = 2
NSW = 0
```

with the PAW_PBE Ni potential and 2x2x2 k -points. Lattice parameters were taken from the materials project website [30].

.2.3 For molecular hydrogen

INCAR:

```
ENCUT = 500
IBRION = 2
ISIF = 2
LCHARG = False
LWAVE = False
NSW = 100
```

with the PAW_PBE H potential and 50 fully automatic k -points. Two H-atoms were placed arbitrarily into a large simulation cell.

.3 Elastic tensors

The resulting elastic tensors from using the stress-strain method in VASP which were used to calculate the elastic moduli are listed in the following:

Hydrogen mostly in Ti-planes (partially relaxed):

```
[[356.0, 152.9, 144.2, -4.2, 4.3, 6.1],
 [152.9, 241.9, 117.1, -34.2, 7.7, -3.1],
 [144.2, 117.1, 266.8, -26.2, 11.8, 7.3],
 [-4.2, -34.2, -26.2, 64.7, 3.8, -1.0],
 [4.3, 7.7, 11.8, 3.8, 77.8, 0.9],
 [6.1, -3.1, 7.3, -1.0, 1.0, 75.1]]
```

Hydrogen mostly in Ti-planes (fully relaxed):

```
[[ 235.5, 103.2, 115.8, 0.8, -3.3, 15.2],  
[ 103.2, 207.6, 114.3, -15.6, 5.7, 10.6],  
[ 115.8, 114.3, 259.2, -12.0, 8.5, 12.7],  
[0.8, -15.6, -12.0, 61.0, 4.3, -1.1],  
[-3.3, 5.7, 8.5, 4.3, 53.0, -5.3],  
[ 15.2, 10.6, 12.7, -1.1, -5.3, 46.6]]
```

Hydrogen mostly in Ni-planes (partially relaxed):

```
[[296.3, 170.7, 158.3, 17.0, 9.8, 2.0],  
[170.7, 269.8, 157.8, -25.7, 10.5, 4.2],  
[158.3, 157.8, 320.1, 1.1, 12.5, 0.3],  
[17.0, -25.7, 1.1, 51.7, -4.2, -1.1],  
[9.8, 10.5, 12.5, -4.2, 68.8, 10.2],  
[2.0, 4.2, 0.3, -1.1, 10.2, 68.5]]
```

Hydrogen mostly in Ni-planes (fully relaxed):

```
[[ 67.2, 73.3, 81.6, -28.7, -32.9, -73.0],  
[ 73.3, -1.3, 50.9, -25.3, -28.4, 1.7],  
[ 81.6, 50.9, 125.2, -12.4, -58.0, -63.6],  
[-28.7, -25.3, -12.4, 6.9, -22.7, -7.6],  
[-32.9, -28.4, -58.0, -22.7, 3.7, 33.4],  
[-73.0, 1.7, -63.6, -7.6, 33.4, -3.5]]
```